Met O (APR) Turbulence and Diffusion Note No. 224

Tropospheric ozone modelled with a global-scale Lagrangian model of diurnal atmospheric chemistry

by

**W.J. Collins, D.S. Stevenson,
C.E. Johnson, R.G. Derwent**

Met O (APR)
(Atmospheric Processes Research)
Meteorological Office
London Road
Bracknell
Berks, RG12 2SZ

Report on work requested by Air Quality Division, Department of the Environment and supported by Contract Number EPG 1/3/17.

Note

This paper has not been published. Permission to quote from it should be obtained from the Assistant Director, Atmospheric Processes Research Division, Met O (APR), Meteorological Office, London Road, Bracknell, Berkshire, RG12 2SZ.

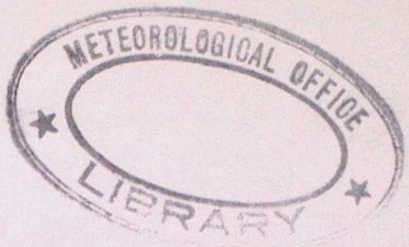

Met O (APR) Turbulence and Diffusion Note No. 224

Tropospheric ozone modelled with a global-scale Lagrangian model of diurnal atmospheric chemistry

by

W.J. Collins, D.S. Stevenson,
C.E. Johnson, R.G. Derwent

Met O (APR)
(Atmospheric Processes Research)
Meteorological Office
London Road
Bracknell
Berks, RG12 2SZ

Report on work requested by Air Quality Division, Department of the Environment and supported by Contract Number EPG 1/3/17.

Note

This paper has not been published. Permission to quote from it should be obtained from the Assistant Director, Atmospheric Processes Research Division, Met O (APR), Meteorological Office, London Road, Bracknell, Berkshire, RG12 2SZ.

Tropospheric ozone modelled with a global-scale Lagrangian model of diurnal atmospheric chemistry

W.J. Collins, D.S. Stevenson, C.E. Johnson and R.G. Derwent

Abstract. A three-dimensional Lagrangian tropospheric chemistry model is used to investigate the impact of human activities on the tropospheric distribution of ozone and hydroxyl radicals. The model describes the behaviour of 50 species including methane, carbon monoxide, oxides of nitrogen, sulphur dioxide and nine organic compounds emitted from human activities and a range of other sources. The chemical mechanism involves about 100 chemical reactions of which 16 are photochemical reactions whose diurnal dependence is treated in full. The model utilises a five minute chemistry time step and a three hour advection time step for the 10,000 air parcels. Meteorological data for the winds, temperatures, clouds and so on are taken from the UK Meteorological Office global model for 1994 onwards. The impacts of a 50% reduction in European NO_X emissions on global ozone, methane and OH radical concentrations are assessed. Surface ozone concentrations decrease in summertime and rise in wintertime, but to different extents. Methane lifetimes lengthen somewhat from 8.2 to 8.4 years in the Northern Hemisphere summer after emission controls.

Key words: global model, Lagrangian, three-dimensional, tropospheric chemistry, ozone, NO_X, emission controls.

Contents

1	Introduction		3
2	The Global 3-D Chemistry Transport Model		4
	2.1	Advection scheme	5
	2.2	Boundary layer height	7
	2.3	Chemistry	7
	2.4	Photolysis	8
	2.5	Emissions	12
	2.6	Deposition	14
	2.7	Model output	15
3	Some model results		15
	3.1	July run	16
	3.2	February run	18
	3.3	Budgets and lifetimes	20
4	European NO_X control and its impacts on tropospheric chemistry		23
	4.1	Summertime conditions	23
	4.2	Wintertime conditions	25
	4.3	Radiative forcing.	26
5	Discussion and evaluation		26
	5.1	Comparison of OH concentrations with observations.	26
	5.2	Comparison of O_3 concentrations with observations.	27
	5.3	Comparison of NO_Y concentrations with observations.	29
6	Conclusions		29

1 Introduction

Over the past few decades, understanding of the behaviour of ozone in the troposphere has changed considerably. Originally, tropospheric ozone was seen as largely controlled by the stratosphere aloft and by destruction at the earth's surface. The formation of photochemical smog in the Los Angeles basin was thought to be a rather localised phenomenon. Levy (1971) drew attention to the importance of the photolysis of tropospheric ozone as a driving mechanism for the chemistry of hydroxyl (OH) and hydroperoxy (HO_2) free radicals linking together the life cycles of methane, carbon monoxide, oxides of nitrogen and ozone. Crutzen (1974) pointed out that tropospheric photochemical production and destruction of ozone were in approximate balance with stratospheric input and surface removal of similar but smaller magnitudes.

Human activities can influence the tropospheric distribution of ozone through a number of mechanisms in addition to the formation of Los Angeles smog in the urban boundary layer (Haagen-Smit *et al.*, 1953). They have influenced the emissions of the major tropospheric source gases: methane (Rasmussen and Khalil 1986; Blake and Rowland 1986), carbon monoxide (Cicerone, 1988), oxides of nitrogen (Crutzen and Gidel 1983; Logan 1985) and hydrocarbons (Hough and Derwent, 1990) which control the tropospheric distribution of hydroxyl radicals and hence ozone production and destruction. Stratospheric ozone depletion leads to decreased exchange of ozone into the troposphere, but perhaps more importantly increased penetration of solar ultraviolet radiation into the troposphere, which all things being equal, would lead to increased tropospheric hydroxyl radical abundances (Thompson and Cicerone, 1986). Furthermore, climate change, driven by the increased radiative forcing due to carbon dioxide, methane and ozone (Fishman *et al.*, 1979) derived from human activities will lead to higher global temperatures, and shifts in relative humidity, cloud distributions and wind patterns and hence may lead to changes in the sources and sinks of tropospheric ozone.

Observational evidence for an increase in tropospheric ozone since preindustrial times has been reviewed elsewhere (IPCC 1995; WMO 1995). Levels are likely to have doubled in the Northern Hemisphere since preindustrial times (Volz and Kley, 1988). Models of the influence of human activities on the coupled life cycles of the tropospheric source gases have shown that they may indeed have caused this observed increase (Hough and Derwent, 1990). The radiative forcing impacts of these changes in tropospheric ozone are significantly smaller than those due to carbon dioxide over the same time period but are comparable to those involving the long-lived trace gases such as methane, nitrous oxide and the chlorofluorocarbons (IPCC, 1995).

It has been pointed out that modelling tropospheric ozone is a difficult task because of the large number of processes involved (IPCC, 1995). Understanding of the emissions of the tropospheric source gases and chemical mechanisms is rudimentary. The key ozone precursor gases are not well-mixed and their im-

pact on the tropospheric ozone life cycle is likely to be spatially variable and inhomogeneous. Most of the models used to study the influence of human activities on tropospheric ozone have been two-dimensional (altitude-latitude) and their relative performances have been evaluated in IPCC (1995) and WMO (1995). Three-dimensional (altitude, latitude and longitude) studies have started to appear (Penner *et al.* 1991; Kasibhatla *et al.* 1993; Jacob *et al.* 1993; Lelieveld and Crutzen 1994) addressing tropospheric ozone. In this paper we extend these three-dimensional high spatial resolution studies of the role of NO_X and ozone chemistry (Kanakidou and Crutzen, 1993) by looking at the role of a range of hydrocarbons and the impact of regional scale NO_X emission reductions on tropospheric ozone.

2 The Global 3-D Chemistry Transport Model

There is a strong case for extending our previous tropospheric ozone modelling from a low resolution two-dimensional model to three-dimensions and so to improve considerably the spatial resolution of the hydrocarbons and NO_X chemistry. So far the main approach to three-dimensional tropospheric chemistry modelling has been Eulerian. In this approach a regular rectangular grid is built throughout the model domain and a finite-differencing scheme is used to describe the processes involved in this fixed framework. The accurate representation of the advection of trace gases is not straightforward if negative concentrations, numerical dispersion and short timesteps are to be avoided (Chock and Winkler 1994; Dabdub and Seinfeld 1994). Pseudospectral techniques offer a formally accurate alternative to the conventional finite difference approach in models of atmospheric dynamics. However, when applied to atmospheric trace gas transport, they may generate negative concentrations and spurious oscillations (Thuburn, 1993).

In this study a Lagrangian approach has been adopted using 10,000 constant mass parcels of air, the centroids of which are advected by interpolated winds from the United Kingdom Meteorological Office UM global circulation model (Cullen, 1993). By this method, all trace gas species are advected together so the chemistry and transport processes can be uncoupled and chemistry timesteps determined locally. There are disadvantages with the Lagrangian approach; species concentrations are defined on parcel centroids but output is generally required on an Eulerian grid and this may be over- or under- determined in a practical implementation where the number of parcels may be limited and distortions due to wind shears can render the notion of a distinct air parcel meaningless.

Our implementation of the Lagrangian approach to three-dimensional chemistry and transport differs in a number of respects from the GRANTOUR model (Taylor 1989; Walton *et al.* 1988; Penner *et al.* 1991) including the handling of diffusion, reinitialisation of particles and the handling of emissions and deposition. The chemical scheme adopted is based on that used with considerable success in developing European regional scale pollution control policies for ozone within the United Nations Economic Commission for Europe EMEP programme (Eliassen *et*

al. 1982; Simpson 1991, 1992a).

2.1 Advection scheme

The height coordinate in the Meteorological Office Unified Model is a hybrid η coordinate. This is derived from the atmospheric pressure at that height and the atmospheric pressure at the surface by the relation:

$$\eta = \frac{P}{P_s} + A\left(\frac{1}{P_0} - \frac{1}{P_s}\right), \tag{1}$$

where P is the pressure, P_s is the surface pressure, P_0 is a reference pressure (=1000 hPa) and A is a coefficient having the dimensions of pressure. Values of A are listed in table I. A is equal to zero near the surface and is equal to the pressure for heights greater than 30 hPa. Near the surface η is terrain-following and is equal to P/P_s, above a height of 30 hPa η follows the pressure surfaces and is equal to $P/(1000\text{ hPa})$.

The Lagrangian cells are advected according to winds taken from the Meteorological Office Unified Model archive, which are based on a grid of 1.25° longitude, 0.8333° latitude and 9 unevenly-spaced η levels between 0.997 and 0.0992 for the horizontal winds (v_U and v_V) and between 0.952 and 0.075 for the vertical wind (v_W). In polar coordinates

$$v_U = R\cos(\theta)\dot{\phi} \quad (\text{in ms}^{-1}), \tag{2}$$

$$v_V = R\dot{\theta} \quad (\text{in ms}^{-1}), \text{ and} \tag{3}$$

$$v_W = \dot{\eta} \quad (\text{in s}^{-1}); \tag{4}$$

where θ and ϕ are the latitude and longitude in radians, and R is the radius of the Earth.

The winds are stored on the archive every six hours which is more data than the program can handle, so every 18 days the 18 day means and standard deviations are calculated for each wind component at each grid point. The period of 18 days was chosen as it is the largest that can be read off the archive at once. Figure 1 shows global winds for a particular η level.

The mean and standard deviation winds for a particular Lagrangian cell are calculated from the cell position using a three dimensional tri-linear interpolation. The wind components are then determined using the mean and a random fraction of the standard deviation.

$$v_i = \bar{v}_i + S_i \times \sigma_i + \frac{1}{2}\nabla_i\sigma_i^2 \; ; \; i = U, V \text{ or } W \tag{5}$$

where $\bar{v}_i$ is the mean wind component, σ_i is the standard deviation of the wind component, S_i is a normally-distributed random number and ∇_i is the i component of the gradient operator. The last term is a drift correction which takes into

account the effect that the cell will tend to drift in the direction of increasing variance. The cell coordinates are updated according to:

$$\theta(t+\Delta T) = \theta(t) + \frac{v_V}{R}\Delta T, \quad (6)$$

$$\phi(t+\Delta T) = \phi(t) + \frac{v_U}{R\cos\theta}\Delta T, \text{ and} \quad (7)$$

$$\eta(t+\Delta T) = \eta(t) + v_W \Delta T, \quad (8)$$

where ΔT is the advection timestep, typically set to three hours.

2.1.1 Convection

Small-scale convective processes (i.e. smaller than can be resolved on the gridded wind data) can have a large influence on the tropospheric chemistry by lifting pollutants out of the boundary layer or bringing down O_3 and NO from the top of the troposphere (Lelieveld and Crutzen, 1994). These subgrid scale convection processes have not yet been included in the model. The 18 day time resolution of the meteorological data also smooths out any synoptic scale convective processes such as depressions and frontal systems, and therefore reduces the effect of convective mixing within the troposphere.

2.1.2 Inter-parcel exchange

During the advection process the Lagrangian cells are considered to be isolated parcels of air. However in reality the air is mixed with other parcels by diffusion processes of the characteristic size of a parcel. In this model the mixing ratio of a species in a parcel c is brought closer to the average background mixing ratio $\bar{c}$ by adding a term $(\bar{c}-c)d$ where d is a parameter representing the degree of exchange (taken to be 0.3). We estimate $\bar{c}$ to be the average mixing ratio of all the cells within a grid volume, which are chosen to be $10^\circ \times 10^\circ \times \Delta\eta = 0.1$ as this gives an average grid volume occupancy of about one and a half cells (more near the equator, less near the poles). The volumes are fixed to the Eulerian grid. Confining the exchange processes to Eulerian grid volumes is perhaps not completely realistic but it does ensure that mass is conserved in the exchange.

The exchange is treated in a more theoretical manner by Walton *et al.* (1988) where the cell mixing ratio is treated as a Gaussian hump on the background with height $c-\bar{c}$ and width σ_0 equal to the cell diameter. In a time interval ΔT this hump spreads to a width $\sigma^2 = \sigma_0^2 + 2K_H\Delta T$ and therefore the height decreases to $(\bar{c}-c)[1-(\sigma_0/\sigma)^2]$ so the exchange parameter d can be identified with $1-(\sigma_0/\sigma)^2$, where K_H is the horizontal grid scale diffusion coefficient. Using $K_H = 10^8$ cm^2 s^{-1} (Walton *et al.*, 1988), and for our model $\Delta T = 10800$s and $\sigma_0 \sim 400$ km, would give $d \sim 0.001$ which is far smaller than our estimate. The background mixing ratios used by Walton *et al.* are from a weighted average of all the cells within a great circle distance of 10° from the centroid of the cell being considered. The weights decrease exponentially with the squares of the distances. This is probably

a more realistic way of estimating the background than in our model but requires N^2 calculations, where N is the number of cells.

Walton *et al.* include grid scale diffusion of the background mixing ratios which is not treated in our model at all.

2.2 Boundary layer height

The height of the boundary layer in our model is estimated from the archived Unified Model meteorological data in two ways based on a study by Maryon and Best (1992). The first is a dry adiabatic method. This involves following the dry adiabatic lapse rate curve up from the near-surface temperature and determining the height at which it intersects the environmental temperature profile. The second is a Richardson number method where the boundary layer height is taken to be the first model layer at which the bulk Richardson number exceeds a critical value. The critical value is usually taken as +0.25 but we use +1.3 as chosen by Maryon and Best (1992) which is more appropriate for the Unified Model output. The boundary layer height used is from the method giving the higher value. In practice the dry adiabatic method tends to be chosen in convective situations and the Richardson number method in stable situations.

2.3 Chemistry

There are 50 species in the model, including the main trace gas species which are thought to influence the tropospheric ozone budget: methane, carbon monoxide, hydrogen, ozone, nitric oxide and nitrogen dioxide, sulphur dioxide, and nine non-methane volatile organic compounds. A wide range of atomic and free radical species have been incorporated in the model, including organic peroxy, alkoxy and carbonyl compounds formed by hydrocarbon oxidation. These model are produced and destroyed in reactions and photochemical dissociations, the rate coefficients for which are specified as functions of temperature and incident light respectively. At present the model includes 90 chemical reactions (see table II) and 16 photochemical reactions (see table III), perfect mixing within a parcel is assumed. The time variation of the concentration of a species X is determined by the differential equation

$$\frac{\mathrm{d}}{\mathrm{d}t}[X] = P - Q[X]$$

where P is the production term (in molecules $\mathrm{cm}^{-3}\ \mathrm{s}^{-1}$) and Q is the relative loss term (in s^{-1}) for species X.

The method used to integrate the differential equation depends on the size of the relative loss term Q compared with the chemical timestep used in the model Δt, and is based on the QSSA method (Hesstvedt *et al.*, 1978).

$$\begin{aligned}
[X] &= [X] + (P - Q[X])\Delta t && , \quad 1/Q > 100\Delta t \\
[X] &= P/Q + ([X] - P/Q)e^{-Q\Delta t} && , \quad 0.1\Delta t < 1/Q < 100\Delta t \\
[X] &= P/Q && , \quad 1/Q < 0.1\Delta t.
\end{aligned}$$

The concentration of each chemical species is updated every chemical timestep, Δt, which is set at 5 minutes in the present study.

2.3.1 The influence of meteorological variables on rate coefficients

The gas-phase chemistry is affected by the humidity, temperature and pressure. The conversion from mixing ratios to concentrations is proportional to the pressure and inversely proportional to the temperature. Most of the rate coefficients depend on the temperature, the coefficient for $HO_2+HO_2 \overset{H_2O,M}{\rightarrow} H_2O_2$ (M is any air molecule) also depends on the humidity. Some reactions involve water vapour explicitly as a reactant.

The temperature and surface pressure are read off the Unified Model archive in the same manner as the wind fields. The pressure at any η level is a function of the surface pressure. The specific humidity fields are retrieved from an ECMWF reanalysis as monthly means on a $10°\times10°\times100$ hPa grid.

2.3.2 Rate coefficient data

The rate coefficient data for the chemical reactions in table II were taken from literature data evaluations. The data for the reactions of the atoms, molecules and free radicals derived from O, H, N, CO and SO_2 were taken from Atkinson *et al.* (1992) and for the hydrocarbon degradation reactions from Atkinson (1994). The reaction $SO_2 \overset{H_2O(\ell)}{\rightarrow}$ Sulphate Aerosol is given a constant reaction rate of $0.01 hr^{-1}$ (Eliassen *et al.*, 1982).

2.4 Photolysis

The most important chemical reactions in the atmosphere are the dissociations driven by sunlight. These can directly break up some of the pollutants emitted into the atmosphere or their derivatives. A more important aspect of photolysis is that it produces free radicals such as OH which will oxidise the larger molecules, to produce chemical species which can be removed from the atmosphere by wet or dry deposition. The photochemical reactions that we are included in our 3D Lagrangian tropospheric chemistry model are listed in table III.

The photolysis rate (J_X) for a species (X) is the product of the spherically integrated (actinic) flux (F) with the absorption cross-section (σ) and the quantum yield (ϕ), integrated over all wavelengths (λ).

$$J_X = \int_0^\infty F(\lambda)\sigma_X(\lambda)\phi_X(\lambda)\mathrm{d}\lambda. \qquad (9)$$

The quantum yield is the probability of the species dissociating after absorbing a photon. In practice the integral is restricted to the range in which the integrand is significant and the integral itself is replaced by a sum over wavelength intervals.

The cross-sections and quantum yields for the reactions have been obtained from a variety of sources (Burkholder *et al.* 1993; Atkinson *et al.* 1992; NASA

1992; Martinez *et al.* 1992; Nicovitch and Wine 1988; Rattigan *et al.* 1992; WMO 1986). The actinic flux is affected by a large number of factors. The solar flux incident on the atmosphere is attenuated by ozone and molecular oxygen absorption. The remaining flux reaching the troposphere is scattered by aerosols, clouds and atmospheric molecules and is reflected by the earth's surface. Thus the light incident on any air parcel has arrived by many different and tortuous paths. Section 2.4.1 will describe a method used to calculate the spherically integrated solar flux at any point.

2.4.1 Calculation of solar fluxes

The algorithm used to calculate the spherically integrated solar flux is an adaptation of the one-dimensional two stream model (upward and downward fluxes) developed by Hough (1988). To approximate the integral in equation 9 the spectrum is divided up into 106 wavelength intervals between 200 and 662.5 nm taken from WMO (1986).

2.4.2 Absorption and scattering

Attenuation A of light by ozone or molecular oxygen is given by:

$$A = \exp(-\int_{\text{path}} \sigma \rho ds), \tag{10}$$

where σ is the photon absorption cross-section for an oxygen or ozone molecule and ρ is the appropriate molecular number density. The integral is along the path travelled by the light. For a homogeneous atmospheric layer i of vertical thickness Δz_i, the attenuation simplifies to:

$$A_i = \exp(-\sigma \rho_i \frac{\Delta z_i}{\cos \theta_i}), \tag{11}$$

where θ_i is the angle the path makes with the vertical in layer i (this will be slightly different from the zenith angle due to refraction). In this model the total oxygen column above the highest layer (70 hPa) is taken to be 3.72×10^{23} molecules cm^{-2}, the ozone column is taken from climatological data as a function of position and time of year. As the absorption cross sections are functions of wavelength so too will be the attenuation factors.

The attenuation due to Rayleigh scattering is also governed by equation 11, in this case σ is the wavelength-dependent scattering probability and ρ is the total atmospheric molecular number density. Unlike molecular absorption, the interacting photons are not lost but are scattered isotropically, half in the forward direction and half backwards relative to the flux direction before scattering.

Aerosols are slightly more complicated to deal with as they both scatter and absorb photons. Combining the work of Demerjian *et al.* (1980) and Braslau and Dave (1973a and 1973b) implies that an aerosol column of 1.97×10^7 particles cm^{-2}

has a scattering optical density of 0.09 and an absorption optical density of 0.01. The effects in the model are found by scaling the aerosol columns at each level by the numbers above. The scattered photons are scattered equally forwards and backwards.

2.4.3 Surface reflection

A fraction of the light reaching the bottom of the model is reflected upwards depending on the surface albedo. At present there are only two classes of albedo in our treatment, 'land' and 'ocean', both functions of wavelength, the ocean albedo is also a function of angle of incidence. The values for 'land' are taken from Demerjian *et al.* (1980) and vary from 5% at short wavelengths to 13% at long wavelengths. Those for 'ocean' are calculated by multiplying the values for land by $1.6 \times \sec(\theta)$, where θ is the solar zenith angle, subject to a maximum increase of a factor of 5.

2.4.4 The effect of clouds

In this model clouds are represented by thin partially reflecting mirrors between the model layers with characteristic wavelength-dependent transmittance $\mathcal{T}$. To allow for partial cloud cover, only a fraction of the light is scattered by the cloud, the rest passes through unaffected. Of the scattered light, a fraction $1 - \mathcal{T}$ is scattered backwards and $\mathcal{T}$ forwards. Random overlap between the clouds is assumed.

The wavelength-dependent transmittance of the cloud layers is calculated by Hough (1988) using data from Atwater and Brown (1974) based on measurements by Haurwitz (1948). This assumes that stratus, cumulus and stratocumulus are classified as low cloud, altostratus and altocumulus as medium cloud and cirrus and cirrostratus as high cloud. The cloud data used in this model are retrieved from the Meteorological Office Unified Model archive.

2.4.5 Parameterising the photolysis results for incorporation into the 3-D chemistry model

Ideally we would like to be able to calculate this term exactly by calculating the flux as in section 2.4.1 and integrating according to equation 9, but to do this for the 10,000 air parcels for every 5 minute timestep would be prohibitive in terms of computing time. We are fortunate that most of the variables on which the photolysis rates depend only vary slowly with time. The factors that affect the photolysis rates are;

- solar flux,
- aerosol content,
- stratospheric oxygen and ozone columns,
- tropospheric oxygen and ozone profiles,

- surface albedo,
- cloud cover,
- height above surface,
- solar zenith angle.

Of these, only the solar zenith angle and the cloud cover vary on a diurnal basis; the rest have a characteristic timescale of a year. Values of $\sec\theta$ are calculated for each air parcel at every chemical time step from its latitude, longitude and time of day.

2.4.6 Parameterisation as a function of zenith angle

The photolysis rates have a very strong dependence on solar zenith angle. From equation 11 the effect of attenuating molecules and aerosols is to reduce the direct flux by a factor $\exp(\text{constant} \times \sec\theta)$. So a reasonable guess at a parameterisation is:

$$J = A \times \exp(-B \times \sec\theta), \tag{12}$$

where θ is the zenith angle and A and B are chosen to get the best approximation to the explicitly calculated photolysis rates. The values for A and B will be different for different photolysis reactions. This is obvious for the scale factor A. The θ-dependence, given by B, will be determined by the variations of cross-sections and quantum yields with wavelength, as the different scattering and absorption processes affect the different wavelengths to a greater or lesser extent. For each reaction, A and B are calculated by constraining the parameterised J value at midday local time to be equal to the explicitly calculated one, and constraining the integrals under the parameterised and explicit curves over the entire 24 hour interval to be equal. The first condition guarantees that for overhead sun, when photolysis reactions are at their fastest, the parameterisation is exact. The second condition ensures that when the sun travels over the range of zenith angles in a day the flux of molecules through the reaction in that day is also exact.

2.4.7 Implementation in the model

A 36×18 grid (10° square) on nine levels spaced by $\Delta\eta$=0.1 is used when calculating the parameters A and B for equation 12 as described in section 2.4.6. For each grid square the As and Bs for each reaction and for each level are calculated, taking into account the stratospheric ozone column, the surface albedo, the cloud cover and the variation of solar zenith angle with time of day. The aerosol profile, stratospheric oxygen column, and tropospheric ozone and oxygen profiles are fixed for all grid squares and are taken from Hough (1988).

The stratospheric ozone is taken from Knight (1994) as a function of latitude and converted to a 10°×10° grid. The surface albedo is calculated from the fraction of the grid square covered by land. The range of zenith angles is calculated for

the latitude of the centre of the grid square and the fitting procedure is used as described in the last paragraph of section 2.4.6. The cloud data is taken from the Meteorological Office global rolling archive as an 18-day average of high, medium, low and convective cloud on a 288 × 216 grid. These are averaged and put into a 10° × 10° × 9 level array. The low cloud is put into level 1 (η=0.9), medium into level 4 (η=0.6) and high into level 6 (η=0.4). Along with the convective cloud data, the average heights (in hPa) of the convective cloud base and top are retrieved. Convective clouds with a vertical extent of less than 100 hPa are put into the appropriate level in the array. Those that extend over more than one model layer are put into the layer corresponding to the base of the cloud.

There is significant variation in cloud cover with time of day, especially for low and convective clouds. This is not surprising as more convection is expected in the early afternoon when the land is at its hottest. The Unified Model fields are archived every six hours (0000, 0600, 1200 and 1800 UTC) so the cloud data are averaged over the 18 days separately for these four times. In the chemistry model four separate sets of rate parameterisations are calculated and are used for all the chemical timesteps within 3 hours either side of the specified times.

2.5 Emissions

Emissions into the model are implemented as an additional term in the production flux, P, for the species in the QSSA method (section 2.3), rather than as a step change in species concentration after a chosen timestep. The emissions used are listed in table IV. The anthropogenic, biomass burning, vegetation, soil, oceans and 'other' are all surface sources based on two-dimensional (latitude, longitude) source maps. Stratospheric sources of ozone and nitric acid are calculated as two-dimensional inputs into the top model layer. The aircraft and lightning NO_X sources are three-dimensional. We use the term 'anthropogenic' in this paper to describe direct emissions from fossil fuel combustion, although man will also have a large influence on biomass burning and (through farming) on vegetation, paddies and animal sources. Aircraft are not included in the 'anthropogenic' emissions but are treated separately. The anthropogenic, paddy, tundra, wetland and 'other animal' sources (see table IV) are based on a yearly average and are constant throughout the year. The other sources vary by calendar month.

The methane emissions in table IV were based on the IPCC (1995) assessment and a total source strength of 485 Tg yr^{-1}. The spatial distributions of the oceans, tundra and wetland sources were estimated from the corresponding distributions of biospheric zones (Olson and Watts, 1982); anthropogenic sources were given the same distribution as NO_X emissions (Dignon, 1992) and biomass burning as that of dimethyl sulphide from the same source (Spiro *et al.*, 1992).

The emissions of non-methane hydrocarbons from human activities, together with their spatial distribution, were taken from Piccot *et al.* (1992). Global emissions from vegetation sources were taken from Hough (1991) and were distributed in space and time as for dimethyl sulphide from the corresponding soil and vege-

tation sources (Spiro *et al.*, 1992).

The entries in table IV for carbon monoxide are based on the literature review by Warneck (1988). Biomass burning and human activities, mainly the exhausts of petrol-engined vehicles, are the largest contributors. This table does not account for the carbon monoxide produced by hydrocarbon oxidation which our study shows to be a somewhat larger secondary source than any of the direct primary emissions, see table VII. The spatial distribution of the anthropogenic sources was taken to be the same as that for NO_X (Dignon, 1992) and biomass burning from Spiro *et al.* (1992).

The principle source of the oxides of nitrogen is fossil fuel combustion and table IV reflects this situation (Logan 1983; Dignon and Hameed 1989). The spatial distribution was taken directly from Dignon (1992).

2.5.1 Model treatment of surface emissions

In our model, surface emissions are added on a $10°\times10°$ grid square basis. This is too coarse ($\sim$1200$\times$800 km at mid-latitudes) to resolve individual centres of pollution but is large enough to give an average cell occupancy of approximately two Lagrangian cells within the boundary layer per grid square in the mid-latitudes. After each advection timestep the surface emissions for a grid square are distributed equally over all the Lagrangian cells that are within the boundary layer in that grid square. If there are no cells within the boundary layer for a particular grid square then the emissions are stored until a cell does pass through.

2.5.2 Isoprene

Isoprene is emitted by vegetation during the day, with the emission rate being positively correlated with temperature (Jacob and Wofsy, 1988). In our model we use the simple approach of emitting isoprene at a constant rate during the day (sunrise to sunset), with no emission at night. The rate is adjusted to give the appropriate total emission over a month for each grid square. These monthly emissions were derived from data on dimethyl sulphide emission from vegetation (Spiro *et al.*, 1992) which were scaled to give 450 Tg yr^{-1} of isoprene.

2.5.3 Lightning and aircraft

Lightning is an important NO_X source in the free troposphere (Turman and Edgar 1982; Franzblau and Popp 1989). We have used the same procedure for calculating the emissions as described in Köhler *et al.* (1995). This used a parameterisation based on model-simulated monthly two-dimensional fields of convective cloud top heights. The emissions were distributed evenly in the vertical between the ground and the convective cloud tops. The total was normalised to give a yearly emission of 5 Tg of N, emitted as NO_2. In comparison, Strand and Hov (1994) suggest a total of 8 Tg yr^{-1} of N emitted in the regions of outflow from thunderclouds rather than distributed evenly in the vertical. The lightning emissions are calculated on a $10°\times10°\times\Delta\eta$ =0.1 grid. If there are no Lagrangian cells within a grid volume

then the emissions in the other volumes are increased to give the correct global emission every timestep.

For the NO_X emissions from civil and military aircraft three-dimensional emissions fields were used (Schumann, 1995) which amounted to 0.85 Tg yr^{-1} of N globally. These are put into the model using the same procedure as for lightning.

2.5.4 Stratospheric sources

Murphy and Fahey (1994) estimate an ozone flux of 450 Tg yr^{-1} from the stratosphere and an NO_Y (NO_Y=NO+NO_2+HNO_3+PAN+$2N_2O_5$) flux of 0.45 Tg (N) yr^{-1}. The upper boundary of our model is set at η=0.1 (~100 hPa) and so the vertical windfields are used to calculate a mass flux across the η=0.1 surface on a 10°×10° grid. Only downward mass fluxes were considered, upward fluxes were set to zero. Monthly zonal mean ozone fields are taken from Hough and Woods (1988) and interpolated to give the ozone mass mixing ratio at 98.5 hPa, which is used to calculate the stratospheric flux. This pressure level was chosen as it gives a total ozone flux of 450 Tg over one year. The NO_Y flux is taken to be one thousandth of the ozone flux by mass (as N). It is emitted into the model as HNO_3.

The emissions are calculated on a 10°×10° grid and distributed equally between all Lagrangian cells that are within a grid square and have η values between 0.2 and 0.1. As with the surface emissions, if there are no Lagrangian cells in which to distribute the emissions then the emissions are stored.

2.6 Deposition

For all cells within the boundary layer the species loss flux due to dry deposition is calculated to be $c \times v_d/H$ where c is the species concentration, v_d is the species deposition velocity and H is the height of the boundary layer. The deposition velocities depend on the location of the cell according to whether the cell is over land or ocean and are the values given in Hough (1991) (see table V). This simple classification could be extended to include differences between tundra, forest, desert etc. At present there is no parameterisation of ice cover. The sea ice and Antarctica are classified as 'ocean', and all other land ice is classified as 'land'. These velocities are 1 m values chosen specifically for the purposes of global-scale modelling. If we assume that species concentrations at 50 m are representative of those throughout the mixed boundary layer then we can convert the deposition velocities at 1 m to give values at 50 m allowing for aerodynamic resistance.

$$\frac{1}{V_{50}} = \frac{1}{V_1} + \frac{50}{K_z} \tag{13}$$

where V_{50} is the deposition velocity at 50 m, V_1 is the deposition velocity at 1 m and K_z is the effective vertical eddy diffusion coefficient in $m^2\ s^{-1}$ between 1 m and 50 m. K_z is approximated by:

$$K_z = 50 \times \frac{k^2 \overline{U}_{30}}{\log \frac{30}{z_0} \log \frac{50}{1}} \tag{14}$$

where $\overline{U}_{30}$ is the average 30 m wind (the lowest Unified Model layer), k is the Von-Karman constant (0.4) and z_0 is the surface roughness length in m. The roughness lengths are taken to be 2×10^{-4} m over sea and 0.2 m over land. Because the winds are 18-day averages and not diurnally varying, the value for K_z is halved over land during the night to take some account of the increase in the stability of the nocturnal boundary layer.

A more detailed calculation is being developed for the aerodynamic resistance using diurnally varying Monin-obukhov lengths and surface wind stresses.

The only model species that are removed by wet scavenging are HNO_3, H_2O_2 and sulphate aerosol and these have a global removal rate below η=0.7 of 0.1 day^{-1}.

2.7 Model output

Although the model itself is Lagrangian, the most useful way to visualise the output is as concentrations on a regular grid. The chosen output grid was $10° \times 10° \times \Delta\eta$=0.1, as used in the emissions and inter-parcel exchange. The species concentration in each 3-D grid box is taken to be the average of all the cells in that box. To smooth out the distributions near the poles and to fill in holes where there are no cells in a grid box, the grid is convolved with a 2-dimensional (longitude-latitude) Gaussian filter with a constant width of 400 km.

As well as the species concentrations it is often useful to see the fluxes through particular reactions. The average flux per cell within each grid box divided by the volume of a cell at a height corresponding to the middle of the box gives the volume-averaged reaction flux in molecules cm^{-3} s^{-1}.

3 Some model results

The main aim of this model is to simulate global ozone production. The main path for ozone production is the oxidation of a hydrocarbon to a peroxy radical. This reacts with NO to give NO_2 which is subsequently photolysed to give an odd oxygen atom (O^3P). The oxygen atom then combines with molecular oxygen to give ozone (Leighton 1961 and Levy 1971). An example of the series of reactions starting with methane is given below.

$$OH + CH_4 + O_2 \rightarrow CH_3O_2 + H_2O \quad (15)$$

$$CH_3O_2 + NO + O_2 \rightarrow NO_2 + HO_2 + HCHO \quad (16)$$

$$HO_2 + NO \rightarrow OH + NO_2 \quad (17)$$

$$NO_2 + h\nu \rightarrow NO + O^3P; O^3P + O_2 \rightarrow O_3 \quad (18)$$

$$\text{net: } CH_4 + 4O_2 \rightarrow 2O_3 + H_2O + HCHO$$

The nitrogen oxides and odd hydrogen radicals are conserved in this mechanism, so the series of reactions will continue to cycle until they are removed by other

means. The most important of these are:

$$NO_2 + OH \rightarrow HNO_3 \quad (19)$$
$$HO_2 + HO_2 \rightarrow H_2O_2 + O_2 \quad (20)$$
$$OH + HO_2 \rightarrow H_2O + O_2. \quad (21)$$

The important ozone destroying reactions are:

$$O_3 + h\nu + H_2O \rightarrow O_2 + 2OH \quad (22)$$
$$O_3 + HO_2 \rightarrow OH + 2O_2 \quad (23)$$
$$O_3 + OH \rightarrow HO_2 + O_2 \quad (24)$$
$$O_3 + NO_2 \rightarrow NO_3 + O_2. \quad (25)$$

To understand the production of ozone therefore we must understand the distribution of the precursors; OH radicals, peroxy radicals and oxides of nitrogen. To achieve this the model simulation was run for two periods; 71 days from 2nd May to 12th July using 1994 meteorological data (summer run), and 70 days from 1st December to 5th February using 1994/1995 meteorological data (winter run).

3.1 July run

Surface and zonal average species mixing ratios of ozone, NO_Y, OH and HO_2 for the July run are shown in figures 2a–h. These mixing ratios are the average values over the last 5 days of the run.

The OH surface distribution is mostly zonal, being in a broad band centred about 20° North near where the solar actinic fluxes are highest. The distribution is not significantly affected by the continents except over equatorial Africa and South America where the isoprene emissions from the forests convert the OH to HO_2. In the zonal average profile, the increased mixing ratio at ~20° north is the most obvious feature. The mixing ratio (molecular density of OH / molecular density of air) increases monotonically with altitude due mainly to the decrease in the density of air with height. In general terms, the molecular density of OH (molecules per unit volume) shows little variation with height throughout the troposphere.

The distribution of NO_Y near the surface follows the land masses as all the surface sources are land-based (anthropogenic, biomass burning and soils). Above the surface, the sources are from lightning and aircraft. The highest concentrations are found in the industrialised regions in the Northern Hemisphere (East Coast of the United States, Central Europe and South East Asia), and above areas of biomass burning and lightning activity in Brazil, Southern Africa and Australia. The zonal average profile of NO_Y shows the vertical extent of the anthropogenic emissions (30°N–65°N) and the natural emissions (30°S–5°S). The emissions from lightning can be clearly seen in the Northern Hemisphere. The major oceans and particularly the Southern Ocean are relatively free of NO_Y at the surface, there

is no production here but the dry deposition of HNO_3 is still efficient. However, higher up in the troposphere where there are few removal processes, the NO_Y is advected into the high southern latitudes and over the oceans.

The HO_2 radical shows a pattern halfway between the zonal OH and the continental NO_Y. This is to be expected since, as we saw with OH, the radical-producing photolysis reactions depend on the solar radiation. However the formation of HO_2 radicals also depends on the presence of pollutants such as hydrocarbons (see for instance equation 16) therefore the distribution follows the continents much more strongly than OH does, in fact over the tropics HO_2 and OH are anticorrelated as the HO_2 producing reactions are straight conversions of OH to HO_2. In the tropics there are no peaks corresponding to the biomass burning as there were for NO_Y. The zonal average profile of HO_2 shows a maximum at the surface centred about 40° north, much further north than in the OH profile. The mixing ratio decreases with height following the water vapour concentration which controls the concentrations of HO_X=(OH+HO_2+2×H_2O_2).

The differences in the spatial distributions of the various ozone precursors justify our rejection of two-dimensional (latitude-altitude) modelling. The correlations between the precursors can only be resolved with a three-dimensional model.

At the surface in the northern mid-latitudes, the ozone distribution follows that of NO_Y and HO_2. There is a strong maximum over the eastern United States and broader maxima over Europe and South East Asia with small ozone maxima in the regions of biomass burning in the southern sub-tropics. The lifetime of ozone at the surface (a few days) is longer than that of NO_Y so the ozone spreads outside the continents more. The major loss for ozone near the surface is dry deposition which is a factor of six less effective over the oceans. The zonal average profile shows a maximum at the surface at the latitude of industrial production and a minimum over the Southern Ocean. The maximum at the top of the troposphere in the Northern Hemisphere is due to stratospheric influx.

The fluxes through the ozone precursor reactions $OH + CH_4 + O_2 \rightarrow CH_3O_2 + H_2O$ and $CH_3O_2 + NO + O_2 \rightarrow NO_2 + HO_2 + HCHO$ are shown in figures 3a–d.

The methane mixing ratio varies by only 20–30% throughout the troposphere, so at the surface the CH_4+OH reaction is controlled entirely by the OH distribution. The flux has a zonal pattern (with a maximum about 20° north) apart from the regions of low flux over equatorial Africa and South America which are caused by high isoprene emissions competing with methane for the OH. The profile of the zonal average flux can best be understood by comparing it with the profile of the OH distribution in molecules cm^{-3} (figure 4a) rather than as a mixing ratio. The OH distribution is mostly columnar, having little variation with height. The region of lower OH concentration just north of the Equator and extending up to $\eta \sim 0.5$ is caused by high clouds, the reduction in OH concentration near the surface is due to enhanced loss by reaction with pollutants. As the CH_4 mixing ratio is almost constant, the molecular density (molecules cm^{-3}) increases with pressure, therefore the CH_4+OH reaction flux is largest at the surface and decreases with

height. The reaction has a strong temperature dependence and so this compounds the rapid fall-off with height. The notch at ~5° north, η ~0.6 in figure 3b is from the cloud-induced OH reduction.

Although the production of CH_3O_2 occurs in a wide zonal band, the next step in the ozone production cycle, which is the reaction of CH_3O_2 with NO (see figure 3c), occurs over the continents and especially over industrial regions and areas of biomass burning. The profile of the zonal average reaction flux (see figure 3d) shows the influence of the surface NO sources but the decrease with height and with latitude south of 30° south is due to the decreasing rate of CH_3O_2 production. These two reactions are the rate-determining ones for ozone production. So we need the combination of the zonal OH, continental NO and height-dependent CH_4 distributions to understand the ozone production pattern.

3.2 February run

The main differences between the summer and winter time conditions are the distribution of sunlight, and the amount and distribution of emitted species. The sunlight, apart from the effects of clouds, is zonally symmetric, the maximum moving from around 20° north in July to around 20° south in February. The biomass burning contribution moves from south of the equator (central South America and Southern Africa) to just north of the equator (central Africa) but the total remains the same. The Northern Hemisphere mid-latitude emissions from vegetation (the most important of these being isoprene) disappear in February, the African and South American sources move further south, and the Australian vegetation emissions reappear. The stratospheric inputs of ozone and HNO_3 are two and a half times higher in February than in July.

In Central Europe, the boundary layer OH mixing ratios are about a factor of five less in February than in July (compare figures 2e and f with 5e and f). On a global scale, the higher OH concentrations have shifted to the Southern Hemisphere. There are minima in the distribution over Brazil and Zaire caused by isoprene emissions converting OH to HO_2. The maximum around the Horn of Africa is in a region of high insolation, little cloud cover and low emissions. There is less OH in the high southern latitudes in February compared to the high northern latitudes in the July run. This is likely to be because there are few NO_X emissions from the Southern Ocean and Antarctica and so little radical production. The February zonal average profile is almost a mirror image of the July one. There are some differences near the equator as the differences in the land distribution north and south of the equator will affect the convective cloud cover and the convective transport of emissions.

The surface distribution of NO_Y (figure 5c) is largely determined by the emissions where the largest seasonal effect is due to the biomass burning. The large areas of high NO_Y concentration over South America, Southern Africa and Australia in figure 2c have disappeared to be replaced by high concentrations in Central Africa and China. The increase in NO_Y over the industrial areas of Europe

and Russia in February is because the removal processes (involving OH and HO_2) are less efficient, rather than any increase in emission. The zonal average profile (figure 5d) shows a broad band of high NO_Y concentrations in the Northern Hemisphere at lower altitudes rather than the separate maxima for industrial and biomass burning latitudes seen in figure 2d.

The maxima in the HO_2 distribution (figure 5g) have shifted into Southern Hemisphere in February. However, unlike the July case, the HO_2 distribution over the continents does not follow the NO_Y distribution as it is the volatile organic compounds (VOCs) which convert OH to HO_2. In the Northern Hemisphere the sources of NO_Y and VOCs are largely anthropogenic and hence coincident. In the Southern Hemisphere the primary route for OH to HO_2 conversion is through isoprene (reaction 251 in table II followed by reactions 242, 243, 252 or 253). Isoprene is emitted from vegetation, in February this comes from the forests of South America, Southern Africa, South East Asia and Australia, whereas the NO_Y comes from biomass burning in Central Africa, Central America and China. The spatial variations in the emissions of different species are well resolved in our model. The zonal average profile (figure 5h) is similar to the July one. The main differences being less HO_2 near the surface and more HO_2 at the top level of the model. The increase at the top level is probably due to the increased downward flux of stratospheric ozone, the decrease at the bottom probably due to less anthropogenic hydrocarbon sources.

The ozone distribution in February (figure 5a) is similar to the equivalent July distribution except in the Northern Hemisphere over the industrial regions. There are no ozone maxima in these regions, in fact over North America there are large holes in the ozone concentration. At the low OH and HO_2 mixing ratios found in the Northern winter the ozone production slows down and the anthropogenic emissions of NO_X remove more ozone than they produce through the titration reactions of ozone with NO and NO_2 (reactions 11 and 12 in table II). In the tropics, the ozone maxima are found at the overlap of the HO_2 and NO_Y distributions as both VOCs and NO are needed to form ozone. In the zonal average profile (figure 5b) the concentrations are lower at the surface in the Northern Hemisphere in February than in July, this is due to the titration effect as explained above. There is however a new ozone peak at the top of the model in the Southern Hemisphere that was not there in July. This feature can not be explained by stratospheric sources, as these are lower in the Southern Hemisphere in February than in July, and is caused by the high concentrations of both NO_Y and HO_2 which lead to significant ozone production.

The fluxes through the precursor reactions $OH + CH_4 + O_2 \rightarrow CH_3O_2 + H_2O$ and $CH_3O_2 + NO + O_2 \rightarrow NO_2 + HO_2 + HCHO$ are shown in figures 6a–d.

As with the July run (figures 3a and b) the CH_4+OH reaction follows the OH distribution closely (see figures 5e and 4b, and figures 6a and b). The same arguments apply to the February CH_3O_2+NO reaction fluxes (figures 6c and d) as in July, there are however elevated concentrations of CH_3O_2 over regions of

isoprene emission as it is one of the products of isoprene breakdown. This leads to higher reaction rates over South America, Southern Africa and Australia than would be expected from the CH_4+OH fluxes.

3.3 Budgets and lifetimes

To gain a better insight into the factors controlling the photochemistry in the model, it is instructive to look at the fluxes through the important reactions. Tables VI–VIII list the global fluxes that comprise the production and loss terms of NO_Y, CO, and O_3, integrated over the last five days of the July run.

The oxides of nitrogen (NO_Y) can be divided into two groups NO_X (NO+NO_2) and NO_Z (NO_3+$2N_2O_5$+HNO_3+PAN). The largest fluxes for NO_Y are the interconversions $NO_X \rightarrow NO_Z$ and $NO_Z \rightarrow NO_X$ (see table VI). The net flux is always to convert NO_X to NO_Z and is roughly a tenth of the interconversion rate. The large difference in the interconversion rates between July and February (almost a factor of two) is mostly due to the stability of PAN in the Northern Hemisphere in the winter. The small (about 20%) difference in the net $NO_X \rightarrow NO_Z$ conversion is due to less formation of organic nitrates from NO_3+isoprene in February, although this is offset by an increase in the winter dry deposition of HNO_3 as more nighttime chemistry converts NO_X to N_2O_5 and then HNO_3.

The greatest source of CO is emission from the surface (see table VII) of which the largest contributions are from anthropogenic emissions and biomass burning (table IV). Unlike the anthropogenic emissions, the biomass burning varies with season although the global totals are not very different in July and February. The next greatest source is photolysis or oxidation of HCHO, this is much stronger in July where there is greater photochemical activity over the Northern Hemisphere. There is a net production of CO in both February and July because the biomass burning emissions are higher than in the previous month in each case.

The global area average photochemical production of ozone in the summer (July) is 2.3×10^{11} molecules cm^{-2} s^{-1}, this compares with a stratospheric input of 2.2×10^{10} molecules cm^{-2} s^{-1} and dry deposition flux of 1.6×10^{11} molecules cm^{-2} s^{-1}. The fluxes for the winter (February) are 1.1×10^{11}, 5.8×10^{10} and 1.0×10^{11} (all in molecules cm^{-2} s^{-1}) for the chemical production, stratospheric influx and dry deposition respectively. If we estimate average annual fluxes by taking the averages of the July and February values then we arrive at fluxes of 1.7×10^{11}, 4.0×10^{10} and 1.3×10^{11} molecules cm^{-2} s^{-1}. The values for production are significantly higher than in Strand and Hov (1994) whereas those for dry deposition are about 15% lower. They give 1.09×10^{11}, 4.1×10^{10} and 1.49×10^{11} molecules cm^{-2} s^{-1} for the chemical production, stratospheric influx and dry deposition respectively.

The total global ozone production can be broken down into the individual production and removal terms as listed in table VIII. Nearly all the photochemical production of ozone is through the photolysis of NO_2 (equation 18) and so it is more useful to look at the production and removal of both O_3 and NO_2. The major production term is the reaction of HO_2 and NO, HO_2 is found over most of the

globe in regions of photochemical radical production. The sum of the production terms representing the RO_2+NO reactions of the two isoprene oxidation products RO_2IP_1 and RO_2IP_2 is the next most important term in July but is less important in February. Of the other peroxy radicals, the flux through CH_3O_2+NO is greater than the total of the fluxes through the remainder of the RO_2+NO reactions. CH_3O_2 is produced by the oxidation of methane throughout the troposphere and over polluted regions by the oxidation of longer chain hydrocarbons. In contrast, the other peroxy radicals tend to be produced over continental areas because they are only produced from non-methane hydrocarbons. The total photochemical loss for ozone is twice the dry deposition flux in July and three times the deposition in February.

It is interesting to investigate which precursors are producing the peroxy radicals (HO_2 and RO_2) that are so necessary for ozone formation. The most important production and loss terms are listed in table IX. From this table it appears that the largest peroxy radical production terms are OH attack on CH_4 and CO. This is because the lifetimes of CH_4 and CO are long enough for them to be spread throughout the troposphere to react in the regions where the OH concentration is high, that is away from continental pollution sources. Of course in these regions the NO_X concentration is so low that the peroxy radicals recombine without producing any ozone. In fact in the ozone producing regions the major source of radicals is from the oxidation and photolysis of HCHO which is derived from CH_3O_2, which in turn comes from the breakdown of non-methane hydrocarbons. In both July and February, isoprene and its oxidation product methyl vinyl ketone (MVK) provide the largest sources of radicals of those formed from oxidation of the non-methane hydrocarbons, although the contribution is less in February. Most of the decrease in peroxy radical production between July and February can be explained by the decrease in isoprene emissions. The major peroxy radical loss in the continental boundary layer is the HO_2+NO reaction with the HO_2+HO_2 recombination also significant. HO_2+HO_2 is more significant in the winter and away from the polluted regions.

Tables X and XI list the total production and loss terms for the VOCs as well as the species lifetimes for the July and February runs. For CO and H_2 the emissions account for approximately half of the production terms, for all the other species the only production term is surface emission. The major removal term for hydrogen is dry deposition, but for all the other species, reaction with OH is the most important. Dry deposition is also a significant removal process for carbon monoxide, and the reactions with ozone are significant for the removal of ethene and propene. Global species lifetimes are calculated by dividing the global total species mass by the removal flux. Methane has by far the longest lifetime of more than eight years, isoprene has the shortest of less than half a day. Of those species

whose primary loss is through OH oxidation, the lifetime is given by:

$$\tau_s = \frac{1}{K_{OH,s} \times \overline{[OH]}_s},$$

where τ_s is the species lifetime, $K_{OH,s}$ is the rate coefficient for the reaction OH+species→..., and $\overline{[OH]}_s$ is the average OH concentration seen by the species. The global average OH concentration is much the same throughout the year but the maximum of the distribution moves from Northern Hemisphere in July to the Southern Hemisphere in February (see figures 4a and b). Methane, the concentration of which has little latitude gradient, has similar lifetimes in July and February. The lifetimes of the reactive anthropogenic hydrocarbons such as n-butane, o-xylene and toluene increase by factors of 3–6 in February because the production is almost exclusively in the industrial northern mid-latitudes where there is a large reduction in the OH concentration in the winter. This is especially true within the continental boundary layer where much of the OH is removed by reaction with pollutants. O-xylene reacts very quickly with OH (summer lifetime = 24 hours) and so does not get out of the boundary layer, as a consequence its lifetime increases by a factor of six in the winter. Species emitted by vegetation show less variation in lifetime with season as the regions of production move from the Northern Hemisphere in July to the Southern Hemisphere in February and so still see high levels of OH. This is most noticable for ethene (for which more than half the emissions are from vegetation) where the lifetime increases by only 40% in February even though it is more reactive than n-butane and toluene. The lifetime of isoprene is complicated by the diurnally varying emissions, scaling the methane lifetime by the ratio of the methane OH reaction coefficient to that of isoprene would give a summer lifetime for isoprene of 3.5 hours.

Figure 7 shows the variation of lifetime with the OH reaction coefficient for the emitted VOCs for July and February. The average OH concentration as seen by the methane is 8.76×10^5 molecules cm^{-3} in July and 8.60×10^5 molecules cm^{-3} in February. This compares with global volume (0–16 km, pole-to-pole) averaged OH concentrations of 13.2 and 13.9×10^5 molecules cm^{-3} in July and February respectively. The difference between the average OH seen by methane and the global volume-averaged OH is large and worthy of comment. In part, it is caused by the large temperature gradient across the troposphere which leads to an order of magnitude decrease in the OH+CH_4 rate coefficient with altitude. Also, because the concentration of methane is approximately proportional to pressure, the OH+CH_4 reaction flux is highest at the surface where the OH concentrations are somewhat depleted. The solid line is drawn with a slope of 1.0 through the point representing the July methane lifetime, a similar line drawn through the February methane lifetime would be indistinguishable from the first. In July the other species lie close to the line demonstrating that they see the same average OH concentration as the methane, the exceptions are hydrogen which has a large dry deposition term and isoprene which has a diurnally varying emission rate. In February only the

species with long lifetimes (ethane and carbon monoxide) lie near the line. Species emitted by vegetation (ethene, propene and isoprene) show a small deviation from the straight line in February with distance from the line increasing with reactivity. Those species that are primarily anthropogenic in origin (n-butane, toluene and o-xylene) show a much larger deviation from the straight line reflecting the strong OH depletion in the continental winter boundary layer.

4 European NO_X control and its impacts on tropospheric chemistry

In order to provide a test for our model, we investigated the effect of an emission control scenario on the model ozone distribution. This scenario was simply a cut in anthropogenic NO_X emissions over Europe by half. The area of Europe was arbitrarily defined as a trapezium bounded in the north and south by the 70°N and 30°N latitude circles, in the west by the 10°W meridian and in the east by a line from 70°N 90°E to 30°N 60°E. This region includes a large part of western Russia. The anthropogenic NO_X sources in the 'European' region average 4.3×10^{10} molecules $cm^{-2}s^{-1}$, with a total mass of 9 Tg (N) yr^{-1} out of a global total of 22 Tg (N) yr^{-1}. The reduction scenario is therefore a cut of 4.5 Tg (N) yr^{-1} or 0.012 Tg (N) day^{-1}. This is not necessarily expected to be a realistic scenario but is useful in testing the model. In practice hydrocarbon emissions would also reduce as most NO_X sources are also sources of hydrocarbons.

4.1 Summertime conditions

After the NO_X control, the total model inventory of NO_Y decreases by 0.042 Tg and of ozone by 4.8 Tg. This gives a molecular ratio of a decrease of 33 molecules of ozone per molecule reduction in NO_Y. The decrease in the NO_Y inventory gives a NO_Y lifetime in the model of 3.5 days. Figures 8a and b show the fractional decrease in ozone by reducing the NO emissions as a surface plot and as a section from the surface to the top of the model at 10°–20° E. At the surface there is a net reduction in ozone of between 10 and 20% over Europe and a small reduction outside Europe particularly where the ozone has been advected round the Arctic. The section shows that the ozone decrease extends up to $\eta \sim 0.6$ over Europe and $\eta \sim 0.3$ over the Arctic. A similar experiment by McKeen *et al.* (1991) for the eastern United States gave an average ozone decrease of 12–16% for a halving of the anthropogenic NO_X emissions. The ozone decrease in our model over central Europe is more than 15%. This larger sensitivity to NO_X emissions is because the strength of the emissions are less ($\sim10\times10^{10}$ molecules cm^{-2} s^{-1} in central Europe compared with 19×10^{10} molecules cm^{-2} s^{-1} used in McKeen *et al.* 1991) giving greater ozone production efficiency, and the emission resolution is coarser in our model which does not adequately resolve the high NO_X emitting industrial centres.

To quantify this more precisely it is instructive to look at the number of ozone molecules reduced per molecule reduction in NO_Y. We use NO_Y rather than NO_X

because the NO_X emitted is continuously oxidised and is in equilibrium with other NO_Y species under steady-state conditions. If we assume that the chemistry is in steady-state then the O_3/NO_Y reduction ratio should tell us how many molecules of ozone are produced by each NO_X molecule before it is oxidised. Figures 9a and b show a surface map and a vertical section of the ratio of the change in ozone to that in NO_Y. Areas where the change in the NO_Y mixing ratio has changed by less than 10 ppt are left blank since there the changes in ozone and NO_Y are so tiny that the signal is swamped by noise. At the surface in the polluted regions over Europe the ratio ranges from about 2 to 10. This is in agreement with results from Olszyna *et al.* (1994) and Trainer *et al.* (1993) who calculated ratios of 10 and 8.5 respectively for rural areas of the United States. In the less polluted regions the ratio increases to up to 100. From figure 9b it can be seen that above $\eta \sim 0.7$ over the polluted region between 20 and 100 ozone molecules are produced before each NO molecule is oxidised. What we see is that the $d[O_3]/d[NO_Y]$ ratio is inversely dependent on the amount of pollution, in particular the NO_Y concentration. This is because the main removal process for NO_X is $OH+NO_2 \rightarrow HNO_3$ which also removes an odd hydrogen radical.

Graphs of the ozone production efficiency against the mixing ratios of NO_Y and OH are shown in figures 10a and b. Each cross on the graph represents one grid volume in the model output. Only those grid volumes where the NO_Y mixing ratio has changed by more than 100 ppt are used (the looser cut on 10 ppt used in figures 9a and b was chosen to allow a better visualisation of the geographical variation of the efficiency). These graphs show a negative dependence on the NO_Y mixing ratio above $[NO_Y] \sim 1$ ppb. Between $[NO_Y]=1$ ppb and $[NO_Y]=10$ ppb the efficiency drops by a factor of 5–10 which is roughly in agreement with the results from Lin *et al.* (1988) after they have included the effects of nighttime removal of NO_3. This suggests that they are correct to assume that all the nighttime NO_3 is lost. We do include the N_2O_5 loss with water vapour $N_2O_5+H_2O(g) \rightarrow HNO_3$ but not the reaction with liquid water on aerosols which would increase the efficiency fall off still further (Dentener and Crutzen, 1993). Although the efficiency is inversely dependent on the NO_Y concentration all the values are still positive which implies that the whole region is in a NO_X-limited regime even for NO_Y levels as high as 10 ppb. This is probably not entirely realistic as ozone production in urban centres is often not NO_X-limited, however our $10° \times 10°$ emission grid is too coarse to resolve these centres and will lead to an overestimate of the total ozone production (Sillman *et al.*, 1990). Simpson (1992b) and (1993) calculated a decrease in mean ozone over Europe in July of 9% after a 50% NO_X reduction (compared with our values of 10–20%), all points showed a reduction in the monthly mean ozone concentrations but a few showed an increase in the maximum July ozone concentrations.

There is no dependence on the OH mixing ratio (figure 10b) which suggests that the reaction chain is not OH-limited.

4.2 Wintertime conditions

In February the decreases in the global inventories are 0.094 Tg and 0.6 Tg for NO_Y and ozone respectively, a ratio of 2 ozone molecules per NO_Y. This gives a NO_Y lifetime of 7.9 days. Even though the NO_Y lifetime has more than doubled compared with the July conditions, the ozone production efficiency has decreased by a factor of about 16. So the effectiveness of the NO_X control in reducing ozone has decreased by a factor of 8. Liu *et al.* (1987) concluded that if nighttime nitrogen chemistry is ignored then the decrease in ozone production efficiency in the winter should be compensated for by the increase in the NO_X (or NO_Y) lifetime, so the ozone production term divided by the NO_X emission rate should be independent of season. They postulate that this will not be the case if nighttime nitrogen chemistry is important, and our results confirm that nighttime chemistry is important in the European winter.

Instead of the main loss rate for NO_X being through the reaction with OH as before, it is now through the reactions $NO+O_3 \rightarrow NO_2$ and $NO_2+O_3 \rightarrow NO_3$, $NO_3+NO_2 \rightarrow N_2O_5$, $N_2O_5+H_2O \rightarrow 2HNO_3$. So in regions of high NO_X and low OH, reducing NO emissions will actually increase the ozone concentrations as there will be less titration of ozone with NO_X. This can be seen in figure 8c which is a surface map of the percentage decrease in ozone after the emission controls. Over Europe all the values are negative i.e. there is an increase in the ozone concentration, however over North Africa, the Middle East and Central Asia the ozone levels are decreased. Reducing the emissions increases the near-surface ozone concentrations by up to 40% in the most polluted areas. South of the polluted regions, the NO_X emission reduction again, as in summertime, leads to a reduction in ozone production. Globally, the total ozone inventory decreases with NO_X emission reduction in wintertime, despite there being local ozone increases over the European continent. The vertical extent of the effect of the emission controls is shown in figure 8d.

Looking at the $d[O_3]/d[NO_Y]$ ratios again in figures 9c and d; over Europe and the Arctic the ratio is between 0 and -2 which agrees with the NO_X-ozone titration principle. Away from the pollution sources and higher in the atmosphere the ratio is positive with values up to 20.

Graphs of the ozone production efficiency (figures 10c and d) show that the efficiency is never positive for NO_Y mixing ratios greater than 3 ppb. For those efficiencies that are negative there seems to be a positive dependence on the NO_Y mixing ratio, increasing from -2 at very low NO_Y mixing ratios to -0.5 at the highest mixing ratio. This is likely to be because in the less polluted regions the reaction sequence $NO+2O_3 \rightarrow NO_3$ will be the dominant loss.

There is a strong positive dependence of the ozone production efficiency on the OH mixing ratio which confirms that lack of OH is a major cause of the ozone destruction in the winter.

4.3 Radiative forcing.

An approximate effect of emission reductions on the global radiative forcing can be calculated from the average ozone mixing ratio change at each level in the model. This can be converted into a radiative forcing term using the method of Lacis *et al.* (1990). The results from our runs show a radiative forcing due to the effect of the emission controls on ozone of $+3\times10^{-3}$ W m^{-2} in the February run and -3×10^{-3} W m^{-2} in July.

5 Discussion and evaluation

Although in a Lagrangian model there is no explicit grid resolution, we have necessarily imposed an artificial resolution. This is most evident for the emission fields; in order to ensure a high probability of finding a cell within the boundary layer over an emission site the sites have to be sufficiently large. For convenience we chose $10°\times10°$, this is far too large to be able to distinguish between rural and urban areas, the area of each square is of the order of a large European country. Therefore our chemistry will in some sense be an average of the conditions in urban, rural and remote areas which makes it difficult to make comparisons with data except in regions where there is little spatial variation in emissions.

Another factor that will influence the chemistry is the time resolution of the meteorology. For a description of the evaluation of the transport processes in our model see Stevenson *et al.* (1995). At present we use 18-day averages for the wind, temperature, cloud and boundary layer fields. This does not fully resolve individual weather systems such as depression tracks which will readily mix the pollutants throughout the depth of the troposphere, or high pressure systems which concentrate pollutants and lead to elevated ozone episodes. At the current model resolution the aim is to model the average monthly chemistry over a large geographical region.

5.1 Comparison of OH concentrations with observations.

The global mean OH concentration in our model is 13.2×10^5 molecules cm^{-3} in July and 13.9×10^5 molecules cm^{-3} in February averaged over the entire model domain, pole-to-pole and 0–16 km. Estimates of the global OH concentration have been made by measurements of the lifetime of methyl chloroform in the troposphere. Prinn *et al.* (1992) calculated a mean tropospheric OH concentration of $8.1\pm0.9\times10^5$ molecules cm^{-3}. This is however not a straightforward volume average but is weighted by the methyl chloroform concentration. Assuming that the methyl chloroform distribution is similar to that of methane, we can compare the mean OH concentration to that calculated from methane destruction, which were 8.8×10^5 molecules cm^{-3} in July and 8.6×10^5 molecules cm^{-3} in February. These numbers agree within the errors.

More recently, Prinn *et al.* (1995) have recalibrated their time series of methyl chloroform measurements. This, when taken with revised estimates of industrial

emissions, has led to a downwards revision of their methyl chloroform lifetime and an upwards revision of their mean tropospheric OH concentration to $9.7\pm0.4\times10^5$ molecules cm^{-3}. These later estimates are now higher than our model calculations, although well within the scope of our errors.

Interestingly, Prinn *et al.* (1995) go on to estimate methane lifetimes of 7.9 ± 0.3 years in the lower atmosphere and 8.8 ± 0.4 for its total atmospheric lifetime (stratospheric loss included). The latter lifetime is directly comparable with our 0–16 km, pole-to-pole, February–July methane lifetime of 8.3 years given in tables X and XI. The agreement here is most heartening and somewhat better than would have been anticipated based on the respective estimates of tropospheric mean OH concentrations. This situation reflects the extreme sensitivity of mean tropospheric OH concentration estimates to the distribution of the trace gases with which they are reacting. Evidently, the three-dimensional distributions of the $OH+CH_4$ and $OH+CH_3CCl_3$ reaction fluxes are different enough to cause significant differences in estimates of spatially-averaged OH concentrations.

5.2 Comparison of O_3 concentrations with observations.

Surface ozone concentrations within the boundary layer tend to be measured a few tens of metres from the ground. This poses a problem for comparisons with our model since, to include enough Lagrangian cells to get a sufficiently accurate horizontal resolution, we average the species mixing ratios over the range η=1.0–0.9 (surface to ~1.0 km). Over the continents, nighttime ozone measurements will be characteristic of the ozone-depleted shallow nocturnal boundary layer (height<0.3 km) whereas the near-surface ozone concentrations in our model will include a large contribution from the free troposphere. Hence the model concentrations will be higher than the diurnal average of the observed concentrations but lower than the daytime values.

Oceanic measurements of ozone will not have the problem with the nocturnal boundary layer and so should agree with the model results. Results from Winkler (1988) for the Atlantic Ocean in table XII show the good agreement with our model in the Southern Hemisphere with July values generally above 20 ppb and February values between 10 and 20 ppb. In the Northern Hemisphere the ozone measurements are in agreement except that they do not show the plume of higher ozone concentrations (>40 ppb) between 30° and 40° N that we have in our model. It is possible that we are advecting too much ozone out from the United States.

A series of ozone measurements from remote sites (Oltmans and Levy, 1994) are listed in table XII (Barrow–South Pole). All of the sites except Izaña have maximum ozone concentrations in the spring and a minimum in the summer, Oltmans and Levy suggest that the summer minimum over the oceans is due to net ozone photochemical destruction by radicals. None of our results except for Barbados reproduce the summer minimum. Comparing our results with those from Barrow, Reykjavik, Bermuda, Cape Grim, Syowa and the South Pole, we consistently underestimate the winter concentrations (February in the Northern Hemisphere

and July in the Southern Hemisphere) and overestimate the summer ones. The overestimation of the summer values can be explained if we are advecting material too far from the continents. Our low winter values are less easy to account for, but it is interesting to note that our calculated concentrations for Mauna Loa are half those measured in either season. Mauna Loa is too remote for this underestimation to be accounted for by underestimations of photochemical production. It could imply that ozone-rich air is being brought down from aloft by advection processes that are not resolved in our model (the Mauna Loa Observatory is at a height of 3.4 km above sea level). Lack of subgrid scale convection may explain our low winter concentrations in remote areas. The seasonality of our calculations over Izaña agrees well with the observations but we underestimate the concentrations by ~5 ppb in both July and February.

Our model reproduces the July ozone concentrations at Cape Point and Elandsfontein in South Africa very well (Combrink *et al.*, 1995) but overestimates the February values in both cases (see table XII).

Observations of ozone concentration at Mace Head in Ireland were classified according to the wind direction (Derwent *et al.*, 1994). Those where the wind came from Europe (NE–S) were termed 'polluted', those with winds from between south west and north were termed 'unpolluted'. Our results agree best with the 'polluted' data (table XII) but this is due to strong advection of polluted air from the eastern United States rather than from Europe.

Measurements of ozone over the Amazon rainforest in July (Gregory *et al.*, 1988) give lower ozone concentrations for the daytime boundary layer (20 ppb) than our model (40 ppb). This is due to two reasons, higher NO_X concentrations in our model due to biomass burning, and lower deposition velocities. The emissions from biomass burning in our model are distributed evenly throughout the boundary layer which leads to high NO_X concentrations particularly at night. In reality, intense heat from the biomass burning causes deep convection, carrying the pollutants high into the troposphere. The dry deposition problem results from our simplistic categorisation of dry deposition regions into 'land' or 'sea', rainforests are much more efficient at removing pollutants than other categories of land. Dry deposition velocities calculated over the Amazon basin by Kaplan *et al.* (1988) are 20 mm s^{-1} for both ozone and NO_2, compared with our model deposition velocities of 6 mm s^{-1} and 1 mm s^{-1} for ozone and NO_2 respectively.

Comparison with observations over regions with very heterogeneous emission distributions is very difficult due to the lack of resolution in the model emission distributions. Results from Virginia in 1989 (Poulida *et al.*, 1991) agree very well in the winter but our model overestimates the summer ozone concentration by a factor of 2–3. 1989 had particularly low ozone concentrations in Virginia (with a maximum 1 hour average of 80 ppb in July) which may account for some of the discrepancy. As this region is not NO_X-limited we are probably losing some of the O_3+NO_2 titration by spreading our emissions over a 10°×10° grid.

European summertime daily maximum ozone concentrations from Simpson

(1993) show a similar geographical distribution to our results but are of the order of 10–20 ppb less. They are mean values for the months April to September and so do not resolve the high ozone production in July.

5.3 Comparison of NO_Y concentrations with observations.

Few measurements of total NO_Y concentrations have been made, some that have are listed in table XIII. In many of these cases, measurements of the constituent NO_Y species can only account for about 60% of the total NO_Y concentration.

Results from Northern Canada (Ontario and Quebec/Labrador in table XIII) (Talbot *et al.*, 1994) were classified according to whether the air was judged to be background air, mixed tropical and background air, or air contaminated by biomass burning. Our results are considerably higher than the observations, even compared with the biomass burning contaminated air. This is due to NO_Y from anthropogenic sources reaching these remote regions in our model. The problem is caused by the lack of resolution in our emissions and output, and too much diffusion. Our results agree well with those from Alaska (Sandholm *et al.*, 1992), largely because this region is distant from any very large anthropogenic NO_X sources.

The model results are generally in good agreement with those from the eastern United States (Brasstown Bald, Whitetop, Bondville, Scotia, Egbert and Whiteface in table XIII) (Parrish *et al.*, 1991) considering the lack of resolution in the NO_X emission fields. The most noticable exception is the measurement from Bondville where very high NO_Y concentrations (up to 20 ppb) build up beneath the nocturnal inversion.

Measurements from more remote areas have been reviewed by Ridley (1991) (Niwot Ridge, Point Arena, east Pacific boundary layer and MLOPEX in table XIII). The model results agree with the measurements from Niwot Ridge but overestimate those from Point Arena and the east Pacific boundary layer, again due to lack of emission resolution and too strong diffusion/advection. The MLOPEX measurements from Mauna Loa are slightly higher than our results which may be due to the height of the observatory (3.4 km) and the fact that the air was sampled in downslope conditions and so is more representative of the free troposphere.

6 Conclusions

A three dimensional Lagrangian model of tropospheric chemistry has been constructed which is driven by emissions, stratospheric concentrations of ozone and other species, and meteorological information. Meteorological fields used were archived from the UK Meteorological Office Unified Model. The model contains a comprehensive description of the gas phase chemistry of around fifty species, and is designed to provide an adequate description of tropospheric ozone and odd hydrogen chemistry. All the model species are integrated in the three- dimensional space, and the diurnal cycle is followed. The actinic fluxes required to define the

photolysis rates are calculated by using cloud amount data archived at a frequency of four times each day. Other meteorological data used by the model include wind data to determine the three-dimensional trajectories of the Lagrangian cells, temperature to determine the thermal rate coefficients, and humidity as a catalyst in HO_2 recombination and a reactant with $O(^1D)$, an important source of free radicals. The profiles of temperature and wind are used to define the boundary layer depth, which in turn, determines whether a particular Lagrangian cell may receive emissions from the surface. The chemical scheme includes a flux algorithm which calculates the amount of material processed by each reaction.

The emissions of NO_X, carbon monoxide, methane, sulphur dioxide, hydrogen, two species of aldehydes and seven hydrocarbons are described from industrial, non-industrial, continental, and oceanic sources. The great range of emission rates over the globe produces large concentration gradients for short-lived compounds such as NO_X. This behaviour is not obtained with a longitudinally averaged two-dimensional model. We have included the chemistry of the major hydrocarbons, which is essential for calculating features of the radical chemistry such as the $OH \leftrightarrow HO_2$ interconversion rate. As reactions of NO with free radicals dominate the photochemical production of ozone, and the reactions of ozone with OH and HO_2 are important destruction processes, it is concluded that the non-methane hydrocarbons are essential elements of any global tropospheric ozone model.

The concentrations of ozone and NO_Y have been compared with the available observations. The model simulates these concentrations well, and there is particularly good agreement over regions where the surface emissions do not vary significantly over a $10° \times 10°$ grid square. Increasing the number of Lagrangian cells in the model will improve the resolution and allow us to test the model more rigorously over industrial countries. In addition to these direct comparisons, the OH concentrations compare well with those derived from methyl chloroform measurements (Prinn *et al.*, 1995), and the model has a similar methane lifetime to that derived from these measurements.

To understand the importance of individual reactions on a global scale, the globally accumulated production and loss terms for ozone, carbon monoxide and NO_Y have been calculated. In July, the net photochemical production of ozone was calculated to be 1.0×10^{35} molecules per day, compared with a stratospheric input at 100 mb of 9.8×10^{33} molecules per day.

As a first step to investigating possible ozone control strategies, the model was used to simulate the changes in ozone resulting from a 50% reduction in European NO_X emissions. The results from this experiment showed a reduction in ozone over Europe by around 10–20% in the summer, but the NO_X emission reduction was shown to have the opposite effect in the winter, increasing the ozone in the same area by up to 40%. These sensitivity studies to NO_X emissions provide an interesting test of the model ozone production chemistry. In particular, the non-linearity of the ozone production efficiency with NO_Y concentration found here agrees well with that reported in other studies.

Acknowledgements

We wish to thank Karl Kitchen, Roy Maryon, Derrick Ryall and David Thomson for help with parameterisations; David Lee (AEA Technology) for help with the emissions; Mike Jenkin and Gary Hayman (AEA Technology) for help with the chemistry; Øystein Hov (University of Bergen) and David Simpson (IVL Gothenburg) with EMEP chemistry and QSSA method. We also acknowledge AQ Division Department of the Environment for their help and encouragement through contract EPG 1/3/17.

References

Atkinson, R., Baulch, D.L., Cox, R.A., Hampson, R.F., Kerr, J.A. and Troe, J., 1992, Evaluated kinetic and photochemical data for atmospheric chemistry. Supplement IV. IUPAC subcommittee on gas kinetic data evaluation for atmospheric chemistry. *J. Phys. Chem. Ref. Data*, **21**, 1125–1568.

Atkinson, R., 1994, Gas phase tropospheric chemistry of organic compounds. *J. Phys. Chem. Ref. Data*, Monograph **2**, 1–216.

Atwater, M.A. and Brown, P.S., 1974, Numerical computations of the latitudinal variation of solar radiation for an atmosphere of varying opacity. *J. Appl. Meteor.*, **13**, 289–297.

Blake, D.R. and Rowland, F.S., 1986, World wide increase in tropospheric methane. *J. Atmos. Chem.*, **4**, 43–62.

Braslau, N. and Dave, J.V., 1973a, Effect of aerosols on the transfer of solar energy through realistic model atmospheres. Part I: Non-absorbing aerosols. *J. Appl. Meteor.*, **12**, 601–615.

Braslau, N. and Dave, J.V., 1973b, Effect of aerosols on the transfer of solar energy through realistic model atmospheres. Part II: Partly-absorbing aerosols. *J. Appl. Meteor.*, **12**, 616–619.

Burkholder, J.B., Talukdar, R. K., Ravishankara, A. R., and Solomon, S., 1993, Temperature dependence of the HNO_3 UV absorption spectrum, submitted to *J. Geophys. Res.*

Chock, D.P. and Winkler, S.L., 1994, A Comparison of advection algorithms coupled with chemistry. *Atmos. Environ.*, **28**, 2659–2675.

Cicerone, R.J., 1988 How has the atmospheric concentration of CO changed? in F.S. Rowland and I.S.A. Isaksen (Ed.) *The changing atmosphere.* pp 44–61. Wiley, New York.

Combrink, J., Diab, R.D., Sokolic, F. and Brunke, E.G., 1995, Relationship between surface, free tropospheric and total column ozone in two contrasting areas in South Africa. *Atmos. Environ.*, **29**, 685–691.

Crutzen, P.J., 1974, Photochemical reactions initiated by and influencing ozone in the unpolluted troposphere. *Tellus*, **26**, 47–57.

Crutzen, P.J. and Gidel, L.T., 1983, A two-dimensional photochemical model of the atmosphere, 2: The tropospheric budgets of the anthropogenic chlorocarbons, CO, CH_4, CH_3Cl and the effect of various NO_X sources on tropospheric ozone. *J. Geophys. Res.*, **88**, 6641–6661..

Cullen, M.J.P., 1993, The unified forecast/climate model. *Meteorological Magazine*, **122**, 81–94, London, UK.

Dabdub, D. and Seinfeld, J.H., Numerical advective schemes used in air quality models — sequential and parallel implementation. *Atmos. Environ.*, **28**, 3369–3385.

Demerjian, K.L., Schere, K.L., and Peterson, J.T., 1980, Theoretical estimates of actinic (spherically integrated) flux and photolytic rate constants of atmospheric species in the lower troposphere. *Advances in Environmental Science and Technology*, **10**, 369–459.

Dentener, F.J. and Crutzen, P.J., 1993, Reaction of N_2O_5 on tropospheric aerosols: Impact on the global distributions of NO_X, O_3, and OH. *J. Geophys. Res.*, **98**, 7149–7163.

Derwent, R.G., Simmonds, P.G. and Collins, W.J., 1994, Ozone and carbon monoxide measurements at a remote maritime location, Mace Head, Ireland, from 1990 to 1992. *Atmos. Environ.*, **28**, 2623–2637.

Dickerson, R.R., Stedman, D.H. and Delany, A.C., 1982, Direct measurements of ozone and nitrogen dioxide photolysis rates in the troposphere. *J. Geophys. Res.*, **87**, 4933–4946.

Dignon, J., 1992, NO_X and SO_X emissions from fossil fuels: A global distribution. *Atmos. Environ.*, **26A**, 1157–1163.

Dignon, J. and Hameed, S., 1989, Global emissions of nitrogen and sulfur oxides from 1860 to 1980. *J. Air Pollut. Control Ass.*, **39**, 180–186.

Eliassen, A., Hov, Ø., Isaksen, I.S.A., Saltbones, J. and Stordal, F., 1982 A Lagrangian long range transport model with atmospheric boundary layer chemistry. *J. Appl. Meteor.*, **21**, 1645–1661.

Fishman, J., Ramanathan, V., Crutsen, P.J. and Liu, S.C., 1979, Tropospheric ozone and climate. *Nature*, **28**, 818–820.

Fransblau, E. and Popp, C.J., 1989, Nitrogen oxides produced from lightning. *J. Geophys. Res.*, **94**, 11089–11104.

Gregory, G.L., Browell, E.V. and Warren, L.S., 1988, Boundary layer ozone: An airborne survey above the Amazon Basin. *J. Geophys. Res.*, **93**, 1452–1468.

Haagen-Smit, A.J., Bradley, C.E. and Fox, M.M., 1953, Ozone formation in photochemical oxidation of organic substances. *Ind. Eng. Chem.*, **45**, 2086–2089.

Haurwitz, B., 1948, Insolation in relation to cloud type. *J. Meteorol.* **5** 110.

Hesstvedt, E., Hov, Ø. and Isaksen, I.S.A., 1978, Quasi-steady-state approximations in air pollution modeling: Comparison of two numerical schemes for oxidant prediction. *Int. J. Chem. kinet.*, **10**, 971–994.

Hough, A.M., 1988, The calculation of photolysis rates for use in global tropospheric modelling studies. *AERE Report R-13259*, HMSO, London.

Hough, A.M., 1991, Development of a two-dimensional global tropospheric model: Model chemistry. *J. Geophys. Res.*, **96**, 7325–7362.

Hough, A.M. and Derwent, R.G., 1990, Changes in the global concentration of tropospheric ozone due to human activities. *Nature*, **344**, 645–660.

Hough, A.M. and Woods, K.J., 1988, Ozone concentrations in the global atmosphere. Analysis of data from the SBUV instrumentation the Nimbus-7 satellite. *AERE Report R-13271*, HMSO, London.

IPCC, 1995, *Climate change 1994. Radiative forcing of climate change.*, Intergovernmental Panel on Climate Change, CUP, Cambridge.

Jacob, D.J. and Wofsy, S.C., 1988, Photochemistry of biogenic emissions over the Amazon forest. *J. Geophys. Res.*, **93**, 1477–1486.

Jacob, D.J., Logan, J.A., Yevich, R.M., Gardner, G.M., Spivakovsky, C.M., Wofsy, S.C., Munger, J.W., Sillman, S., Prather, M.J., Rodgers, M.O., Westberg, H and Zimmerman, P.R., 1993, Simulation of summertime ozone over North America. *J. Geophys. Res.*, **98**, 14797–14816.

Kanakidou, M. and Crutsen, P.J., 1993, Scale problems in global tropospheric chemistry modeling: Comparison of results obtained with a three-dimensional model, adopting longitudinally uniform and varying emissions of NO_X and NHMC. *Chemosphere*, **26**, 787–801.

Kaplan, W.A., Wofsy, S.C. and Keller, M., 1988, Emission of NO and deposition of O_3 in a tropical forest system. *J. Geophys. Res.*, **93**, 1389–1395.

Kasibhatla, P.S., Levy, H., Moxim, W.J. and Chameides, W.L., 1993, The relative impact of stratospheric photochemical production on tropospheric NO_Y levels: a model study. *J. Geophys. Res.*, **96**, 18631–18636.

Knight, J.R., 1994, Private communication.

Köhler, I., Sausen, R. and Gallardo Klenner, L., 1995, NO_x production by lightning. In U. Schumann (ed.) *The impact of NO_x emissions from aircraft upon the atmosphere at flight altitudes 8-15 km (AERONOX)*

Lacis, A.A., Wuebbles, D.J. and Logan, J.A., 1990, Radiative forcing of climate by changes in the vertical distribution of ozone. *J. Geophys. Res.*, **95**, 9971–9981.

Leighton, P.A., 1961, *Photochemistry of air pollution*, Academic Press, New York.

Lelieveld, J. and Crutsen, P.J., 1994, Role of deep cloud convection the ozone budget of the troposphere. *Science*, **264**, 1759–1761.

Levy, H., 1971, Normal atmosphere: large radical and formaldehyde concentrations predicted. *Science*, **173**, 141–143.

Lin, X., Trainer, M. and Liu, S.C., 1988, On the nonlinearity of the tropospheric ozone production. *J. Geophys. Res.*, **93**, 15879–15888.

Liu, S.C., Trainer, M., Fehensfeld, F.C., Parrish, D.D., Williams, E.J., Fahey, D.W., Hübler, G. and Murphy, P.C., 1987, Ozone production in the rural troposphere and the implications for regional and global ozone distributions. *J. Geophys. Res.*, **92**, 4191–4207..

Logan, J.A., 1983, Nitrogen oxides in the troposphere: Global and regional budgets. *J. Geophys. Res.*, **88**, 10785–10807..

Logan, J.A., 1985, Tropospheric ozone, seasonal behaviour, trends and anthropogenic influence. *J. Geophys. Res.*, **90**, 10463–10482.

Martines, R.D., Buitrago, A.A., Howell, N.W., Hearn, C.H.G. and Joens, J.A., 1992, The near UV absorption spectra of several aliphatic aldehydes and ketones at 300K. *Atmos. Environ.*, **26A**, 185–792.

Maryon, R.H. and Best, M.J., 1992, 'NAME', 'ATMES' and the boundary layer problem. *Met O (APR) turbulence and diffusion note*, No. **204**

McKeen, S.A., Hsie, E.-Y. and Liu, S.C., 1991, A study of the dependence of rural ozone on ozone precursors in the eastern United States. *J. Geophys. Res.*, **196**, 15377–15394.

Murphy, D.M. and Fahey, D.W., 1994, An estimate of the flux of stratospheric reactive nitrogen and ozone into the troposphere. *J. Geophys. Res.*, **99**, 5325–5332.

NASA Panel for Data Evaluation, 1992, *Chemical Kinetics Data for use in Stratospheric Modeling*, Evaluation Number **9**. JPL Publications 92-20.

Nicovitch, J.M. and Wine, P.H., 1988, Temperature-dependent absorption cross sections for hydrogen peroxide vapour. *J. Geophys. Res.*, **93**, 2417–2421.

Olson, J. and Watts, J., 1982 *Map of major world ecosystem complexes*, Environmental Sciences Division, Oak Ridge Nat. Lab., Tenn.

Olszyna, K.J., Bailey, E.M., Simoniatis, R. and Meagher, J.F., 1994, O_3 and NO_Y relationships at a rural site. *J. Geophys. Res.*, **99**, 14557–14563.

Oltmans, S.J. and Levy, H. II, 1994, Surface ozone measurements from a global network. *Atmos. Environ.*, **28**, 9–24.

Parrish, D.D., Buhr, M.P., Trainer, M., Norton, R.B., Shimshock, J. P., Fehsenfeld, F.C., Anlauf, K.G., Bottenheim, J.W., Tang, Y.Z., Wiebe, H.A., Roberts, J.M., Tanner, R.L., Newman, L., Bowersox, V.C., Olszyna, K.J., Bailey, E.M., Rodgers, M.O., Wang, T., Berresheim, H., Roychowdhury, U.K. and Demerjian, K.L., 1991, The total reactive oxidised nitrogen levels and the partitioning between the individual species at six rural sites in eastern North America. *J. Geophys. Res.*, **98**, 2927–2939.

Penner, J.E., Atherton, C.S., Dignon, J., Ghan, S.J., Walton, J.J. and Hameed, S., 1991, Tropospheric nitrogen: A three-dimensional study of sources, distributions and deposition. *J. Geophys. Res.*, **96**, 959–990.

Penner, J.E., Atherton, C.S. and Graedel, T.E., 1994, Global emissions and models of photochemically active compounds. In R.G. Prinn (ed.) *Global atmospheric-biospheric chemistry*, Plenum Press, New York.

Piccot, S.D., Watson, J.J. and Jones, J.W., 1992, A global inventory of volatile organic compound emissions from anthropogenic sources. *J. Geophys. Res.*, **97**, 9897–9912.

Poulida, O., Dickerson, R.R., Doddridge, B.G., Holland, J.Z., Wardel, R.G. and Watkins, J.G., 1991, Trace gas concentrations and meteorology in rural Virginia 1. Ozone and carbon monoxide. *J. Geophys. Res.*, **96**, 22461–22475.

Prinn, R., Cunnold, D., Simmonds, P., Alyea, F., Boldi, R., Crawford, A., Fraser, P., Gutsler, D., Hartley, D., Rosen, R. and Rasmussen, R., 1992, Global average concentration and trend for hydroxyl radicals deduced from ALE/GAGE trichloroethane (methyl chloroform) data for 1978–1990. *J. Geophys. Res.*, **97**, 2445–2462.

Prinn, R.G., Weiss, R.F., Miller, B.R., Huang, J., Alyea, F.N., Cunnold, D.M., Fraser, P.B., Hartley, D.E. and Simmonds, P.G., 1995, Atmospheric trends and lifetime of trichloroethane and global average hydroxyl radical concentrations based on 1978–1994 ALE/GAGE measurements. Submitted to *Science*, February 1995.

Rasmussen, R.A. and Khalil, M.A.K., 1986, 4. Atmospheric methane in the real and ancient atmospheres: concentrations and interhemispheric gradient. *J. Geophys. Res.*, **89**, 11599–

11605..

Rattigan, O., Lutman, E., Jones, R. L., Cox, R. A., Clemitshaw, K., and Williams, J., 1992, Temperature-dependent absorption cross sections of gaseous nitric acid and methyl nitrate, *J. Photochem. Photobiol. A: Chem.*, **66**, 313–326.

Ridley, B.A., 1991, Recent measurements of oxidised nitrogen compounds in the troposphere. *Atmos. Environ.*, **25A**, 1905–1926.

Sandholm, S.T., Bradshaw, J.D., Chem, G., Singh, H.B., Talbot, R. W., Gregory, G.L., Blake, D.R., Sachse, G.W., Browell, E.V., Barrick, J.D.W., Shipham, M.A., Bachmeier, A.S. and Owen, D., 1992, Summertime tropospheric observations related to N_xO_y distributions and partitioning over Alaska: Arctic Boundary Layer Expedition 3A. *J. Geophys. Res.*, **97**, 16481–16509.

Schumann, U. (1995) The impact of NO_X emissions from aircraft upon the atmosphere at flight altitudes 8-15 km (AERONOX). *CEC Report*, Brussels, Belgium.

Sillman, S., Logan, J.A. and Wofsy, S.C., 1990, A regional scale model for ozone in the United States with sub-grid representation of urban power plant plumes. *J. Geophys. Res.*, **95**, 5731–5748.

Simpson, D., 1991, Long period modelling of photochemical oxidants in Europe. *EMEP MSC-W Note 1/91*, The Norwegian meteorological Institute, Oslo.

Simpson, D., 1992a, Long period modelling of photochemical oxidants in Europe. *EMEP MSC-W Note 1/92*, The Norwegian meteorological Institute, Oslo.

Simpson, D., 1992b, Long-period modelling of photochemical oxidants in Europe. Model calculations for July 1985. *Atmos. Environ.*, **26A**, 1609–1634.

Simpson, D., 1993, Photochemical model calculations over Europe for two extended summer periods: 1985 and 1989. Model results and comparison with observations. *Atmos. Environ.*, **27A**, 921–943.

Spiro, P.A., Jacob, D.J. and Logan, J.A., 1992, Global inventory of sulfur emissions with $1° \times 1°$ resolution. *J. Geophys. Res.*, **97**, 6023–6036.

Stevenson, D.S., Johnson, C.E., Collins, W.J. and Derwent, R.G., 1995, Changes to tropospheric oxidants from aircraft nitrogen oxide emissions studied with a 3-D Lagrangian model. *submitted to Atmospheric Environment*

Strand, A. and Hov, Ø, 1994, A two-dimensional global study of tropospheric ozone production. *J. Geophys. Res.*, **99**, 22877–22895.

Talbot, R.W., Bradshaw, J.D., Sandholm, S.T., Singh, H.B., Sachse, G. W., Collins, J., Gregory, G.L., Anderson, B., Blake, D., Barrick, J., Browell, E.V., Klemm, K.I., Lefer, B.L., Klemm, O., Gorselska, K., Olson, J., Herlth, D. and O'Hara, D., 1994, Summertime distribution and relations of reactive odd nitrogen species an NO_Y in the troposphere over Canada. *J. Geophys. Res.*, **99**, 1863–1885.

Taylor, J.A., 1989, A stochastic Lagrangian atmospheric transport model to determine global CO_2 sources and sinks — a preliminary discussion. *Tellus*, **41B**, 272–285.

Thompson, A.M. and Cicerone, R.J., 1986, Possible perturbations to atmospheric CO, CH_4 and OH. *J. Geophys. Res.*, **91**, 10853–10864.

Trainer, M., Parrish, D.D., Buhr, M.P., Norton, R.B., Fehsenfeld, F.C., Anlauf, K.G., Bottenheim, J.W., Tang, Y.Z., Wiebe, H.A., Roberts, J.M., Tanner, R.L., Newman, L., Bowersox, V.C., Meagher, J.F., Olszyna, K.J., Rodgers, M.O., Wang, T., Berresheim, H., Demerjian, K.L. and Roychowdhury, U.K., 1993, Correlation of ozone with NO_Y in photochemically aged air. *J. Geophys. Res.*, **98**, 2917–2925.

US Standard Atmosphere, 1976, US Government Printing Office, Washington DC.

Thuburn, J., 1993, Multidimensional flux-limited advection schemes. *UGAMP Technical Report*, **32**, UK Universities Global Atmospheric Modelling Programme.

Turman, B.N. and Edgar, B.C., 1982, Global lightning distributions at dawn and dusk. *J. Geophys. Res.*, **87**, 1191–1206.

Vols, A. and Kley, D., 1988, Evaluation of the Montsouris series of ozone measurements made in the nineteenth century. *Nature*, **332**, 240–242.

Walton, J., MacCracken, M., Ghan, S., 1988, A global-scale Lagrangian trace species model of transport, transformation, and removal processes. *J. Geophys. Res.*, **93**, 8339–8354.

Warneck, P., 1988, *Chemistry of the natural atmosphere*, pp. 158–170, Academic Press, San Diego, California.

Winkler, P., 1988, Surface ozone over the Atlantic Ocean. *J. Atmos. Chem.*, **7**, 73–91.

WMO, 1986, Atmospheric Ozone 1985, assessment of our understanding of the processes controlling its present distribution and change, *Global Ozone Research and Monitoring Project*, Report No. 16. World Meteorological Organisation, Geneva.

WMO, 1995, Scientific assessment of ozone depletion: 1994. *World Meteorological Organisation. Global Ozone Research and Monitoring Project-Report* No. **37**, Geneva.

Fig. 1. Average horisontal wind velocity vectors at a height of $\eta = 0.8$ (mean pressure above oceans $\sim$ 800 hPa, height above ground $\sim$ 2.0 km) for half of the globe, over the period 1–18 November 1993. Arrow lengths correspond to trajectories of approximately 1 day.

Fig. 2. Near surface and sonal average profiles of mixing ratios of OH, NO_Y, HO_2 and O_3 after a 71 day run ending on 12th July. The values are the average mixing ratios over the last 5 days of the run.

Fig. 3. Near surface and sonal average profiles of fluxes through the reactions $OH + CH_4 + O_2 \rightarrow CH_3O_2 + H_2O$ and $CH_3O_2 + NO + O_2 \rightarrow NO_2 + HO_2 + HCHO$ after a 71 day run ending on 12th July. The values are the average fluxes over the last 5 days of the run.

Fig. 4. Zonal average profiles of the OH molecular density: (a) after a 71 day run ending on 12th July, and (b) after a 70 day run ending on 5th February. The values are the averaged over the last 5 days of the run.

Fig. 5. Near surface mixing ratios of O_3, NO_Y, OH and HO_2 after a 70 day run ending on 2nd February using full European NO emissions. The values are the average mixing ratios over the previous 24 hours.

Fig. 6. Near surface and sonal average profiles of fluxes through the reactions $OH + CH_4 + O_2 \rightarrow CH_3O_2 + H_2O$ and $CH_3O_2 + NO + O_2 \rightarrow NO_2 + HO_2 + HCHO$ after a 70 day run ending on 5th February. The values are the average fluxes over the last 5 days of the run.

Fig. 7. Lifetimes of the hydrocarbons and other tropospheric trace gases in the 3-D model plotted against their OH + trace gas rate coefficients evaluated at 280 K.

Fig. 8. Fractional decrease in ozone mixing ratio, using a reduced European NO emission scenario compared with the same run using full NO emissions: (a) surface, July, (b) section, July, (c) surface, February, (d) section, February.

Fig. 9. Change in ozone mixing ratio divided by the change in NO_Y mixing ratio, between the two runs with different NO emission scenarios: (a) surface, July, (b) section, July, (c) surface, February, (d) section, February. Only values where the NO_Y mixing ratio has changed by more than 100 parts per trillion (100 ppt) are used.

Fig. 10. Ozone production efficiency, defined as the change in ozone divided by the change in NO between the two runs, against the NO_Y and OH mixing ratios without emission controls: (a) and (b) July, (c) and (d) February. Values plotted are for all the grid points where the change in NO_Y mixing ratio was greater than 100 ppt.

Model output level	η	A (hPa)	Mean pressure (hPa)	Approximate height (km)
1	1.0–0.9	0.0–0.0	1013–912	0.0–1.0
2	0.9–0.8	0.0–4.2	912–810	1.0–2.0
3	0.8–0.7	4.2–24.0	810–709	2.0–3.0
4	0.7–0.6	24.0–57.9	709–607	3.0–4.2
5	0.6–0.5	57.9–96.3	607–505	4.2–5.6
6	0.5–0.4	96.3–128.8	505–404	5.6–7.2
7	0.4–0.3	128.8–146.9	404–302	7.2–9.2
8	0.3–0.2	146.9–136.7	302–201	9.2–11.8
9	0.2–0.1	136.7–89.1	201–100	11.8–16.2

TABLE I

Table of the coefficient A used in model to calculate the hybrid height coordinate η, and the pressures and approximate heights of the layers used for the model output. The coefficient A is based on that used in the Meteorological Office Unified Model GCM. The mean pressure is appropriate for the oceans with mean sea level pressure of 1013 hPa, for η close to 1.0 the pressure will be significantly less over high ground. The approximate height is based on a surface pressure of 1013 hPa and a temperature profile taken from the U.S. Standard Atmosphere (1976). Close to the ground the height corresponds to the height above the ground, but at the smaller η values corresponds to the height above the 1000 hPa surface.

$O(^3P) + O_2 + M$	→	$O_3 + M$	$K_1 = 6.0 \times 10^{-34}(T/300)^{-2.3}$
$O(^3P) + NO + M$	→	$NO_2 + M$	K_5 complex
$O(^1D) + N_2$	→	$O(^3P) + N_2$	$K_{7a} = 3.2 \times 10^{-11}\exp(70/T)$
$O(^1D) + O_2$	→	$O(^3P) + O_2$	$K_{7b} = 1.8 \times 10^{-11}\exp(110/T)$
$H_2O + O(^1D)$	→	$2OH$	$K_8 = 2.2 \times 10^{-10}$
$NO + O_3$	→	$NO_2 + O_2$	$K_{11} = 2.0 \times 10^{-12}\exp(-1400/T)$
$NO_2 + O_3$	→	$NO_3 + O_2$	$K_{12} = 1.2 \times 10^{-13}\exp(-2450/T)$
$OH + O_3$	→	$HO_2 + O_2$	$K_{13} = 1.6 \times 10^{-12}\exp(-940/T)$
$HO_2 + O_3$	→	$OH + 2O_2$	$K_{14} = 1.1 \times 10^{-14}\exp(-500/T)$
$NO + NO_3$	→	$2NO_2$	$K_{15} = 1.1 \times 10^{-11}\exp(170/T)$
$HO_2 + NO$	→	$OH + NO_2$	$K_{17} = 3.7 \times 10^{-12}\exp(250/T)$
$NO_2 + NO_3$	→	$NO + NO_2 + O_2$	$K_{19} = 4.5 \times 10^{-14}\exp(-1260/T)$
$NO_2 + NO_3 + M$	→	$N_2O_5 + M$	K_{20} complex
$NO_2 + OH + M$	→	$HNO_3 + M$	K_{21} complex
$2NO_3$	→	$2NO_2 + O_2$	$K_{27} = 1.0 \times 10^{-12}\exp(-2450/T)$
$N_2O_5 + M$	→	$NO_2 + NO_3 + M$	K_{29} complex
$OH + HO_2$	→	$H_2O + O_2$	$K_{30} = 4.8 \times 10^{-11}\exp(250/T)$
$H_2O_2 + OH$	→	$HO_2 + H_2O$	$K_{31} = 2.9 \times 10^{-12}\exp(-160/T)$
$NO_3 + H_2O_2$	→	$HNO_3 + HO_2$	$K_{32} = 4.1 \times 10^{-16}$
$H_2 + OH$	→	$HO_2 + H_2O$	$K_{33} = 5.5 \times 10^{-12}\exp(-2000/T)$
$HNO_3 + OH$	→	$NO_3 + H_2O$	K_{35} complex
$2HO_2 + M$	→	$H_2O_2 + O_2 + M$	K_{36} complex
$SO_2 + OH + M$	→	$HO_2 + SA + M$	K_{39} complex
$SO_2 + CH_3O_2$	→	$SA + HCHO + HO_2$	$K_{40} = 4.0 \times 10^{-17}$
$H_2O + N_2O_5$	→	$2HNO_3$	$K_{42} = 2.0 \times 10^{-21}$
$OH + CH_4$	→	$CH_3O_2 + H_2$	$K_{59} = 2.9 \times 10^{-12}\exp(-1820/T)$
$CH_3O_2 + NO$	→	$HCHO + HO_2$	$K_{60} = 4.2 \times 10^{-12}\exp(180/T)$
$2CH_3O_2$	→	$2HCHO + 2HO_2$	K_{61} complex
$2CH_3O_2$	→	$2HCHO$	K_{62} complex
$CH_3O_2 + HO_2$	→	CH_3O_2H	$K_{65} = 4.1 \times 10^{-13}\exp(790/T)$
$HCHO + OH$	→	$HO_2 + CO$	$K_{66} = 1.0 \times 10^{-11}$
$NO_3 + HCHO$	→	$HNO_3 + CO + HO_2$	$K_{67} = 5.8 \times 10^{-16}$
$CO + OH$	→	$HO_2 + CO_2$	K_{70} complex
$C_2H_6 + OH$	→	$C_2H_5O_2$	$K_{71} = 7.8 \times 10^{-12}\exp(-1020/T)$
$NO + C_2H_5O_2$	→	$CH_3CHO + HO_2 + NO_2$	$K_{72} = 4.9 \times 10^{-12}\exp(180/T)$
$CH_3O_2 + C_2H_5O_2$	→	$2HO_2 + HCHO + CH_3CHO$	$K_{73} = 1.0 \times 10^{-13}$
$CH_3CHO + OH$	→	CH_3COO_2	$K_{75} = 5.6 \times 10^{-12}\exp(310/T)$
$CH_3COO_2 + NO_2 + M$	→	$PAN + M$	K_{77} complex
$PAN + M$	→	$CH_3COO_2 + NO_2 + M$	K_{78} complex
$NO + CH_3COO_2$	→	$CH_3O_2 + NO_2$	$K_{79} = 2.0 \times 10^{-11}$
$CH_3O_2 + CH_3COO_2$	→	$HO_2 + HCHO + CH_3O_2 + CO_2$	K_{80} complex
$nC_4H_{10} + OH$	→	$secC_4H_{10}$	$K_{81} = 1.5 \times 10^{-17}T^2\exp(190/T)$
$NO + secC_4H_{10}$	→	$HO_2 + NO_2 + CH_3COC_2H_5$	K_{83a} complex
	→	$NO_2 + C_2H_5O_2 + CH_3CHO$	K_{83b} complex
$CH_3O_2 + secC_4H_{10}$	→	$2HO_2 + HCHO + CH_3COC_2H_5$	K_{84a} complex
	→	$HO_2 + CH_3CHO + HCHO + C_2H_5O_2$	K_{84b} complex
$CH_3COC_2H_5 + OH$	→	$CH_3COCHO_2CH_3$	$K_{86} = 3.24 \times 10^{-17}T^2\exp(414/T)$
$2C_2H_5O_2$	→	$2CH_3CHO + 2HO_2$	K_{90} complex

TABLE II

Reactions used in the chemistry model. (continued on next page...)

$2CH_3COO_2$	→	$2CH_3O_2 + 2CO_2 + O_2$	$K_{91} = 2.8 \times 10^{-12}\exp(530/T)$
$CH_3COO_2 + CH_3O_2$	→	$2HCHO + O_2$	$K_{92} = 1.0 \times 10^{-13}$
$NO + CH_3COCHO_2CH_3$	→	$HO_2 + CH_3COCOCH_3 + NO_2$	$K_{105} = 5.0 \times 10^{-12}$
$CH_3O_2 + CH_3COCHO_2CH_3$	→	$HCHO + CH_3COCOCH_3 + 2HO_2$	K_{106} complex
$C_2H_4 + OH + M$	→	$CH_2O_2CH_2OH+M$	K_{109} complex
$NO + CH_2O_2CH_2OH$	→	$HO_2 + 2HCHO + NO_2$	$K_{110} = 9.0 \times 10^{-12}$
$CH_3O_2 + CH_2O_2CH_2OH$	→	$3HCHO + 2HO_2$	$K_{111} = 1.0 \times 10^{-13}$
$C_2H_4 + O_3$	→	$CO + 2HO_2 +$ products	$K_{112} = 1.2 \times 10^{-14}\exp(-2630/T)$
$O_3 + C_3H_6$	→	$HCHO + CH_3O_2 + CO + HO_2$	$K_{123} = 4.0 \times 10^{-15}\exp(-1900/T)$
$O_3 + C_3H_6$	→	$CO + CH_3CHO + HO_2$	$K_{124} = 2.6 \times 10^{-15}\exp(-1900/T)$
$OH + C_3H_6 + M$	→	$CH_3CHO_2CH_2OH + M$	K_{125} complex
$NO + CH_3CHO_2CH_2OH$	→	$HCHO + CH_3CHO + HO_2 + NO_2$	$K_{126} = 9.0 \times 10^{-12}$
$CH_3O_2 + CH_3CHO_2CH_2OH$	→	$2HCHO + CH_3CHO + HO_2$	$K_{127} = 1.0 \times 10^{-13}$
$CH_4 + NO_3$	→	$HNO_3 + CH_3O_2$	$K_{200} = 1.0 \times 10^{-18}$
$C_2H_6 + NO_3$	→	$HNO_3 + C_2H_5O_2$	$K_{201} = 1.4 \times 10^{-18}$
$nC_4H_{10} + NO_3$	→	$HNO_3 + secC_4H_{10}$	$K_{202} = 6.6 \times 10^{-17}$
$C_2H_4 + NO_3$	→	RNC_2H_4	$K_{203} = 5.43 \times 10^{-12}\exp(-3401/T)$
$RNC_2H_4 + NO$	→	$ORGNIT + HO_2 + NO_2$	$K_{204} = 1.4 \times 10^{-11}\exp(-180/T)$
$C_3H_6 + NO_3$	→	RNC_3H_6	$K_{205} = 9.45 \times 10^{-15}$
$RNC_3H_6 + NO$	→	$ORGNIT + HO_2 + NO_2$	$K_{206} = 1.4 \times 10^{-11}\exp(-180/T)$
$CH_3CHO + NO_3$	→	$HNO_3 + CH_3COO_2$	$K_{208} = 1.44 \times 10^{-12}\exp(-1862/T)$
$C_5H_8 + NO_3$	→	RNC_5H_8	$K_{209} = 3.03 \times 10^{-12}\exp(-440/T)$
$RNC_5H_8 + NO$	→	$ORGNIT + HO_2 + NO_2$	$K_{210} = 1.4 \times 10^{-11}\exp(-180/T)$
oXYLENE + NO_3	→	$ROXYL_1$	$K_{211} = 3.8 \times 10^{-16}$
$ROXYL_1 + NO$	→	$ORGNIT + HO_2 + NO_2$	$K_{212} = 1.4 \times 10^{-11}\exp(-180/T)$
$NO + TOLP_1$	→	$MEMALDIAL + GLYOX + HO_2 + NO_2$	$K_{213} = 4.1 \times 10^{-12}$
oXYLENE + OH	→	$OXYL_1$	$K_{230} = 1.37 \times 10^{-11}$
$NO + OXYL_1$	→	$HO_2 + MGLYOX + MEMALDIAL + NO_2$	$K_{231} = 4.0 \times 10^{-12}$
MEMALDIAL + OH	→	$MEMALDIAL_1$	$K_{232} = 5.6 \times 10^{-11}$
$MEMALDIAL_1 + NO$	→	$HO_2 + MGLYOX + GLYOX + NO_2$	$K_{233} = 9.0 \times 10^{-12}$
OH + TOLUENE	→	$TOLP_1$	$K_{234} = 5.96 \times 10^{-12}$
$oXYL_1 + CH_3O_2$	→	$2HO_2 + HCHO + MGLYOX + MEMALDIAL$	$K_{240} = 1.0 \times 10^{-13}$
$MEMALDIAL_1 + CH_3O_2$	→	$2HO_2 + HCHO + MGLYOX + GLYOX$	$K_{241} = 1.0 \times 10^{-13}$
$RO_2IP_1 + CH_3O_2$	→	$2HO_2 + HCHO + MVK$	$K_{242} = 1.0 \times 10^{-13}$
$RO_2IP_2 + CH_3O_2$	→	$2HO_2 + HCHO + MGLYOX$	$K_{243} = 1.0 \times 10^{-13}$
$C_5H_8 + OH$	→	RO_2IP_1	$K_{251} = 2.54 \times 10^{-11}\exp(410/T)$
$NO + RO_2IP_1$	→	$HCHO + MVK + HO_2 + NO_2$	$K_{252} = 1.4 \times 10^{-11}\exp(-180/T)$
OH + MVK	→	RO_2IP_2	$K_{253} = 4.13 \times 10^{-12}\exp(452/T)$
$NO + RO_2IP_2$	→	$HO_2 + HCHO + MGLYOX + NO_2$	$K_{254} = 1.4 \times 10^{-11}\exp(-180/T)$
SO_2	→	SA	$K_{255} = 2.77 \times 10^{-6}$
SA	→	wet removal	$K_{256} = 1.16 \times 10^{-6}$

TABLE II

..continued from previous page) Reactions used in the chemistry model. Rate coefficients are in olecules^{-1} cm^3 s^{-1}, except for K_{255} and K_{256} which are in s^{-1}.

$O_3 + h\nu$	→	$O(^3P) + O_2$	($\lambda > 300$ nm)	$J_1 = 4.76 \times 10^{-4}$
$O_3 + h\nu$	→	$O(^1D) + O_2$	($\lambda < 300$ nm)	$J_2 = 3.24 \times 10^{-5}$
$NO_2 + h\nu$	→	$O(^3P) + NO$		$J_3 = 9.00 \times 10^{-3}$
$H_2O_2 + h\nu$	→	$2OH$		$J_4 = 7.98 \times 10^{-6}$
$HNO_3 + h\nu$	→	$OH + NO_2$		$J_5 = 7.12 \times 10^{-7}$
$HCHO + h\nu$	→	$CO + 2HO_2$		$J_6 = 3.30 \times 10^{-5}$
$HCHO + h\nu$	→	$CO + H_2$		$J_7 = 4.99 \times 10^{-5}$
$CH_3CHO + h\nu$	→	$CO + CH_3O_2 + HO_2$		$J_8 = 5.16 \times 10^{-6}$
$CH_3COC_2H_5 + h\nu$	→	$CH_3COO_2 + C_2H_5O_2$		$J_9 = 4.20 \times 10^{-6}$
$CH_3COCOCH_3 + h\nu$	→	$2CH_3COO_2$		$J_{10} = 2.75 \times 10^{-4}$
methyl glyoxal $+ h\nu$	→	$CH_3CHO + CO$		$J_{11} = 1.28 \times 10^{-4}$
glyoxal $+ h\nu$	→	$HCHO + CO$		$J_{12} = 5.76 \times 10^{-5}$
$NO_3 + h\nu$	→	$O_2 + NO$		$J_{13} = 2.39 \times 10^{-2}$
$NO_3 + h\nu$	→	$O(^3P) + NO_2$		$J_{14} = 1.64 \times 10^{-1}$
$N_2O_5 + h\nu$	→	$NO_2 + NO_3$		$J_{15} = 4.61 \times 10^{-5}$
$CH_3O_2H + h\nu$	→	$HCHO + OH + HO_2$		$J_{16} = 4.36 \times 10^{-6}$

TABLE III

Photochemical reactions, and their photolysis rate coefficients, that are implemented in the 3D chemistry model, with sample values in s^{-1} for a solar zenith angle of 15°, with a cloudless sky, over land, 350 Dobson Units of ozone, at an altitude of 0.5 km.

Species	Source								
	Anthropogenic	Biomass Burning	Vegetation	Soil	Oceans	Aircraft	Lightning	Stratosphere	Other
NO_x	22.0	8.0	—	5.0	—	0.85	5.0	—	—
SO_2	63.0	2.2	—	—	15.0	—	—	—	—
HCHO	1.0	—	—	—	—	—	—	—	—
H_2	20.0	20.0	—	5.0	5.0	—	—	—	—
CH_3CHO	0.3	—	—	—	—	—	—	—	—
CO	650.0	800.0	75.0	—	—	—	—	—	—
CH_4	155.0	40.0	—	—	10.0	—	—	—	280.0
C_2H_6	3.5	—	15.0	—	—	—	—	—	—
C_4H_{10}	47.0	—	8.0	—	—	—	—	—	—
C_2H_4	17.0	—	20.0	—	—	—	—	—	—
C_3H_6	21.0	—	20.0	—	—	—	—	—	—
C_5H_8	—	—	450.0	—	—	—	—	—	—
o-xylene	4.7	—	—	—	—	—	—	—	—
toluene	14.0	—	—	—	—	—	—	—	—
HNO_3	—	—	—	—	—	—	—	0.45	—
O_3	—	—	—	—	—	—	—	450.0	—

TABLE IV

Emissions in Tg yr^{-1}, except NO_x and HNO_3, which are in Tg (N) yr^{-1}, and SO_2, which are in Tg (S) yr^{-1}. For the VOCs, any biomass burning contribution is included with the anthropogenic component. The 'Other' for methane includes paddys (60 Tg yr^{-1}), tundra (50 Tg yr^{-1}), wetlands (65 Tg yr^{-1}), termites (20 Tg yr^{-1}) and other animals (85 Tg yr^{-1}).

Species	Land	Ocean
NO_2	1.0	0.5
SO_2	5.0	1.0
CO	0.3	0
O_3	6.0	1.0
HNO_3	40	10
H_2O_2	10	10
H_2	0.45	0
CH_3O_2H	5.0	5.0
PAN	2.0	0

TABLE V

Deposition velocities (in mm s^{-1}) for all the dry deposited species in the model. Values are effective velocities for 1 m above the surface.

Reactive nitrogen (NO_Y)	Flux (molecules/5 days)	
	July	February
Production		
Surface emission of NO_X	2.399×10^{34}	2.335×10^{34}
NO_X from lightning and aircraft	3.65×10^{33}	3.69×10^{33}
Stratospheric input of NO_Z	1.7×10^{32}	4.4×10^{32}
Total production	2.781×10^{34}	2.748×10^{34}
Interconversions		
$NO_Z \rightarrow NO_X$	3.0498×10^{35}	1.7173×10^{35}
$NO_X \rightarrow NO_Z$	3.2790×10^{35}	1.9052×10^{35}
net $NO_X \rightarrow NO_Z$	2.292×10^{34}	1.879×10^{34}
Removal		
NO_2 deposition	9.6×10^{32}	1.70×10^{33}
HNO_3 deposition	1.432×10^{34}	1.865×10^{34}
PAN deposition	2.02×10^{33}	9.8×10^{32}
Organic nitrate formation	9.00×10^{33}	3.24×10^{33}
Total removal	2.630×10^{34}	2.457×10^{34}
Net NO_Y production	1.51×10^{33}	2.91×10^{33}

TABLE VI

Reactive nitrogen (NO_Y) budget.

Carbon monoxide				
Reaction			Flux (molecules/5 days)	
			July	February
Production				
$HCHO+h\nu$	→	$CO+2HO_2$	1.418×10^{35}	9.82×10^{34}
$HCHO+h\nu$	→	$CO+H_2$	2.449×10^{35}	1.692×10^{35}
$CH_3CHO+h\nu$	→	$CO+CH_3O_2+HO_2$	1.11×10^{34}	5.4×10^{33}
methyl-glyoxal$+h\nu$	→	$CO+CH_3CHO$	7.53×10^{34}	3.11×10^{34}
glyoxal$+h\nu$	→	$HCHO+CO$	2.9×10^{33}	3.1×10^{33}
$HCHO+OH$	→	HO_2+CO	1.493×10^{35}	1.206×10^{35}
NO_3+HCHO	→	$HNO_3+CO+HO_2$	2×10^{32}	1×10^{32}
$C_2H_4+O_3$	→	$CO+2HO_2$	2.9×10^{33}	1.5×10^{33}
$O_3+C_3H_6$	→	$HCHO+CH_3O_2+CO+HO_2$	2.6×10^{33}	1.6×10^{33}
$O_3+C_3H_6$	→	$CO+CH_3CHO+HO_2$	1.7×10^{33}	1.0×10^{33}
Emission			5.820×10^{35}	6.034×10^{35}
Total production			1.2147×10^{36}	1.0352×10^{36}
Removal				
$CO+OH$	→	HO_2	8.506×10^{35}	8.313×10^{35}
Deposition			1.141×10^{35}	9.75×10^{34}
Total removal			9.647×10^{35}	9.288×10^{35}
Net production			2.500×10^{35}	1.064×10^{35}

TABLE VII
CO budget.

Ozone Reaction			Flux (molecules/5 days) July	February
		Production		
HO_2+NO	→	$OH+NO_2$	7.97×10^{35}	6.63×10^{35}
CH_3O_2+NO	→	HO_2+NO_2+HCHO	1.49×10^{35}	1.28×10^{35}
RO_2IP_1+NO	→	HO_2+NO_2+products	7.9×10^{34}	3.3×10^{34}
RO_2IP_2+NO	→	HO_2+NO_2+products	7.2×10^{34}	2.8×10^{34}
RO_2+NO	→	HO_2+NO_2+products	1.04×10^{35}	6.6×10^{34}
$NO+NO_3$	→	$2NO_2$	4×10^{33}	3×10^{33}
$NO_3+h\nu$	→	$NO_2+O(^3P)$	1.7×10^{34}	1.3×10^{34}
Stratospheric influx			4.9×10^{34}	1.27×10^{35}
NO_2 emissions			4×10^{33}	4×10^{33}
Total production			1.328×10^{36}	1.068×10^{36}
		Removal		
$O_3+h\nu+H_2O$	→	$2OH$	2.40×10^{35}	2.68×10^{35}
O_3+HO_2	→	$OH+2O_2$	3.50×10^{35}	2.58×10^{35}
O_3+OH	→	HO_2	1.42×10^{35}	1.25×10^{35}
O_3+NO_2	→	NO_3+O_2	2.8×10^{34}	1.9×10^{34}
O_3+olefins	→		7×10^{33}	4×10^{33}
O_3 dry deposition			3.52×10^{35}	2.15×10^{35}
NO_2 dry deposition			1×10^{33}	2×10^{33}
PAN dry deposition			2×10^{33}	1×10^{33}
Total removal			1.123×10^{36}	9.11×10^{35}
Production/Removal			1.18	1.17

TABLE VIII

Major osone production and removal terms.

RO_2 production	Flux (molecules/5 days) July	February
reactions with OH		
H_2	8.6×10^{34}	8.7×10^{34}
H_2O_2	1.22×10^{35}	1.26×10^{35}
O_3	1.42×10^{35}	1.25×10^{35}
CO	8.51×10^{35}	8.31×10^{35}
CH_4	2.76×10^{35}	2.72×10^{35}
C_2H_6	7×10^{33}	5×10^{33}
n-C_4H_{10}	8×10^{33}	8×10^{33}
C_2H_4	1.1×10^{34}	8×10^{33}
C_3H_6	7×10^{33}	6×10^{33}
C_5H_8	8.0×10^{34}	3.3×10^{34}
toluene	1×10^{33}	1×10^{33}
HCHO	1.49×10^{35}	1.21×10^{35}
CH_3CHO	8.8×10^{34}	4.6×10^{34}
$CH_3COC_2H_5$	4×10^{33}	3×10^{33}
methyl maleic dialdehyde	2×10^{33}	2×10^{34}
methyl vinyl ketone	7.9×10^{34}	3.4×10^{34}
Total OH → RO_2	1.914×10^{36}	1.708×10^{36}
Reactions with NO_3		
C_5H_8	9×10^{33}	3×10^{33}
others	2×10^{33}	1×10^{33}
Total NO_3 → RO_2	1.1×10^{34}	4×10^{33}
photolysis		
(2×) HCHO	1.42×10^{35}	9.8×10^{34}
(2×) CH_3CHO	1.1×10^{34}	5×10^{33}
(2×) $CH_3COCOCH_3$	4×10^{33}	3×10^{33}
CH_3O_2H	1.492×10^{35}	1.39×10^{35}
Total photolysis	4.56×10^{35}	3.52
Total production	2.386×10^{36}	2.065×10^{36}
Loss		
HO_2+O_3	3.50×10^{35}	2.58×10^{35}
HO_2+NO	7.97×10^{35}	6.63×10^{35}
HO_2+OH	1.21×10^{35}	1.26×10^{35}
(2×) HO_2+HO_2	3.53×10^{35}	3.27×10^{35}
(2×) $HO_2+CH_3O_2$	1.85×10^{35}	1.69×10^{35}
(2×) $CH_3O_2+CH_3O_2$	1×10^{33}	1×10^{33}
(2×) $CH_3O_2+CH_3COO_2$	2.0×10^{34}	1.2×10^{34}
Total loss	2.384×10^{36}	2.065×10^{36}

TABLE IX

HO_2 and RO_2 production terms.

Volatile organic compounds					
Species	Production molecules/5 days	Removal molecules/5 days	Net production molecules/5 days	Species Mass molecules	Lifetime
hydrogen	4.986×10^{35}	4.939×10^{35}	4.7×10^{33}	5.34×10^{37}	541 days
carbon monoxide	1.215×10^{36}	9.65×10^{35}	2.50×10^{35}	7.2×10^{36}	37 days
methane	2.591×10^{35}	2.769×10^{35}	-1.78×10^{34}	1.66×10^{38}	8.23 years
ethane	7.58×10^{33}	6.78×10^{33}	8.0×10^{32}	7.5×10^{34}	55 days
n-butane	8.44×10^{33}	8.34×10^{33}	-1.0×10^{32}	9.4×10^{33}	5.6 days
ethene	1.445×10^{34}	1.443×10^{34}	2×10^{31}	5.1×10^{33}	1.8 days
propene	1.181×10^{34}	1.188×10^{34}	-7×10^{31}	1.0×10^{33}	10 hours
isoprene	8.797×10^{34}	8.850×10^{34}	-5.3×10^{32}	6.3×10^{33}	8.5 hours
o-xylene	3.59×10^{32}	3.62×10^{32}	-3×10^{30}	7.2×10^{31}	24 hours
toluene	1.25×10^{33}	1.26×10^{33}	-1×10^{31}	6.6×10^{32}	2.6 days

TABLE X
July lifetimes

Volatile organic compounds					
Species	Production molecules/5 days	Removal molecules/5 days	Net production molecules/5 days	Species Mass molecules	Lifetime
hydrogen	4.314×10^{35}	4.235×10^{35}	7.9×10^{33}	5.30×10^{37}	626 days
carbon monoxide	1.035×10^{36}	9.29×10^{35}	1.06×10^{35}	8.0×10^{36}	43 days
methane	2.631×10^{35}	2.731×10^{35}	-1.00×10^{34}	1.67×10^{38}	8.35 years
ethane	3.72×10^{33}	4.60×10^{33}	-8.8×10^{32}	5.7×10^{34}	62 days
n-butane	7.55×10^{33}	7.56×10^{33}	-1×10^{31}	2.4×10^{34}	16 days
ethene	8.91×10^{33}	9.05×10^{33}	-1.4×10^{32}	4.6×10^{33}	2.5 days
propene	8.25×10^{33}	8.37×10^{33}	-1.2×10^{32}	1.8×10^{33}	1.1 days
isoprene	3.613×10^{34}	3.623×10^{34}	-1.0×10^{32}	3.3×10^{33}	11 hours
o-xylene	3.72×10^{32}	4.04×10^{32}	-3.2×10^{31}	5.0×10^{32}	6.2 days
toluene	1.27×10^{33}	1.35×10^{33}	-8×10^{31}	2.0×10^{33}	7.4 days

TABLE XI
February lifetimes

Location	Observations		Model results	
	July	February	July	February
Atlantic (80°N–70°N)	23	—	25–30	15–20
Atlantic (70°N–60°N)	30	—	25–30	15–20
Atlantic (60°N–50°N)	28	21	25–40	15–20
Atlantic (50°N–40°N)	25	30	40–50	20–30
Atlantic (40°N–30°N)	25	30	20–25	30–35
Atlantic (30°N–20°N)	25	28	25–30	30–35
Atlantic (20°N–10°N)	25	24	25–30	25–30
Atlantic (10°N–0°N)	—	20	20–25	25–30
Atlantic (0°S–10°S)	—	12	20–25	15–20
Atlantic (10°S–20°S)	—	15	25–30	20–25
Atlantic (20°S–30°S)	—	12	25–30	15–25
Atlantic (30°S–40°S)	15	15	20–25	15–20
Atlantic (40°S–50°S)	20	12	15–20	15–20
Atlantic (50°S–60°S)	20	10	10–15	10–15
Atlantic (60°S–70°S)	21	10	5–10	10–15
Atlantic (70°S–80°S)	—	10	10–15	15–20
Barrow	22±3	30±4	25–30	5–10
Reykjavik	20±5	35±5	40–50	10–20
Bermuda	21±6	40±6	60–80	35–40
Isaña	48±8	41±4	35–40	30–35
Mauna Loa	39±8	42±6	20–25	20–25
Barbados	19±2	25±3	25–30	30–35
Samoa	19±6	9±1	5–10	5–10
Cape Grim	32	18	15–20	20–25
Syowa	36	18	10–15	20–25
South Pole	35±3	20±2	15–20	15–20
Cape Point	25±3	16±4	25–30	25–30
Verkykopp	40±12	22±10	30–35	30–35
Elandsfontein	38±8	21±7	35–40	30–35
Mace Head (unpolluted)	34	35	50–60	15–25
Mace Head (polluted)	40	24	50–60	15–25
Amazonia	20–30	—	40–45	30–35
Virginia	44±8	27±6	100–120	25–30

TABLE XII

Comparison of ozone measurements with model calculations. Values are all ozone mixing ratios in ppb. Model results are for the heights η=0.9–1.0. Observations from the Atlantic are taken from Winkler (1988); those from Barrow, Reykjavik, Bermuda, Isaña, Mauna Loa, Barbados, Samoa, Cape Grim, Syowa and the South Pole are taken from Oltmans and Levy (1994). The data from Cape Point and Elandsfontein are from Combrink *et al.* (1995). Data from Mace Head are from Derwent *et al.* (1994), those from Amazonia from Gregory *et al.* (1988), and from Virginia from Poulida *et al.* (1991). All data have been estimated from the published graphs rather than tables of values. Where errors have been quoted, these encompass 50% of the data (25th–75th percentiles). The ranges for the model results reflect the spatial resolution in the output and do not represent any detailed error analysis.

Location	Period	Observations	Model results
Northern Ontario (background)	July/August	0.165±0.042	1–2
Northern Ontario (biomass burning)	"	0.395±0.160	1–2
Northern Quebec/Labrador (background)	"	0.185±0.053	0.5–1.0
Northern Quebec/Labrador (mixed)	"	0.082±0.031	0.5–1.0
Northern Quebec/Labrador (biomass burning)	"	0.242±0.083	0.5–1.0
Alaska	"	0.370±0.170	0.3–0.4
Brasstown Bald	August/September	3.2±1.1	4–6
Whitetop	"	2.9±1.5	6–7
Bondville	August	14^{+4}_{-10}	5–6
Scotia	July/August	5±3	6–8
Egbert	August	4^{+4}_{-3}	6–8
Whiteface	September	4±3	8–9
Niwot Ridge	June/July	1.3±0.7	1.5–2.0
Point Arena	April/May	0.5±0.2	1.3–1.5
East Pacific boundary layer	August	0.13±0.05	0.2–1.0
MLOPEX	May	0.27±0.13	0.15–0.20

TABLE XIII

Comparison of NO_Y measurements with model calculations. Values are all NO_Y mixing ratios in ppb. The periods are the months over which the measurements were made, the model results are all for July. Model results are for the heights η=0.9–1.0. Observations from Ontario and Quebec/Labrador are taken from Talbot *et al.* (1994). Those from Alaska are taken from Sandholm *et al.* (1992). The data from Brasstown Bald, Whitetop, Bondville, Scotia, Egbert and Whiteface are from Parrish *et al.* (1991) and the values quoted are means read off the published graphs with errors encompassing 67% of the data. Data from Niwot Ridge, Point Arena, East Pacific boundary layer and MLOPEX are from Ridley (1991), again the values quoted are means read off the published graphs with errors encompassing 67% of the data. The ranges for the model results reflect the spatial resolution in the output and do not represent any detailed error analysis.

Fig. 1. Average horizontal wind velocity vectors at a height of $\eta = 0.8$ (mean pressure above oceans $\sim$ 800 hPa, height above ground $\sim$ 2.0 km) for half of the globe, over the period 1–18 November 1993. Arrow lengths correspond to trajectories of approximately 1 day.

Fig. 2. Near surface and zonal average profiles of mixing ratios of OH, NO_Y, HO_2 and O_3 after a 71 day run ending on 12th July. The values are the average mixing ratios over the last 5 days of the run.

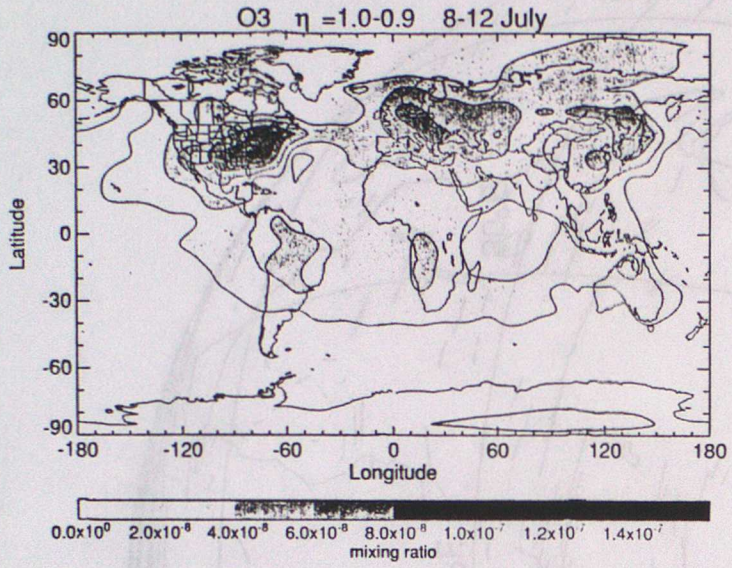

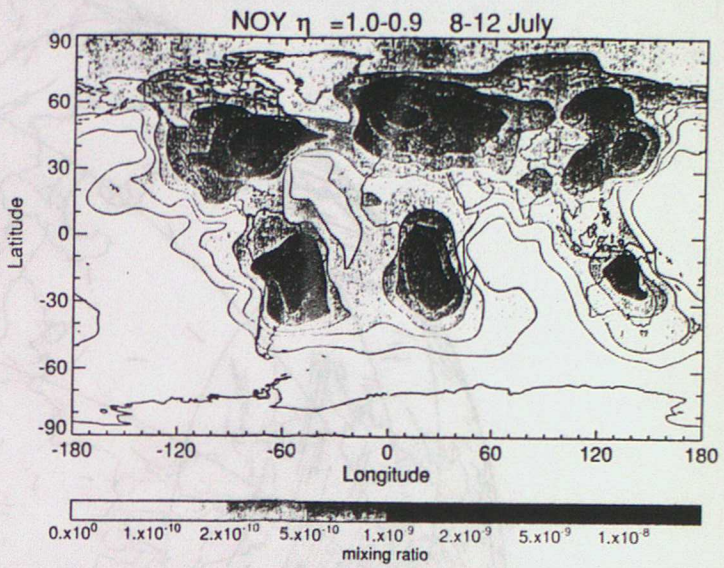

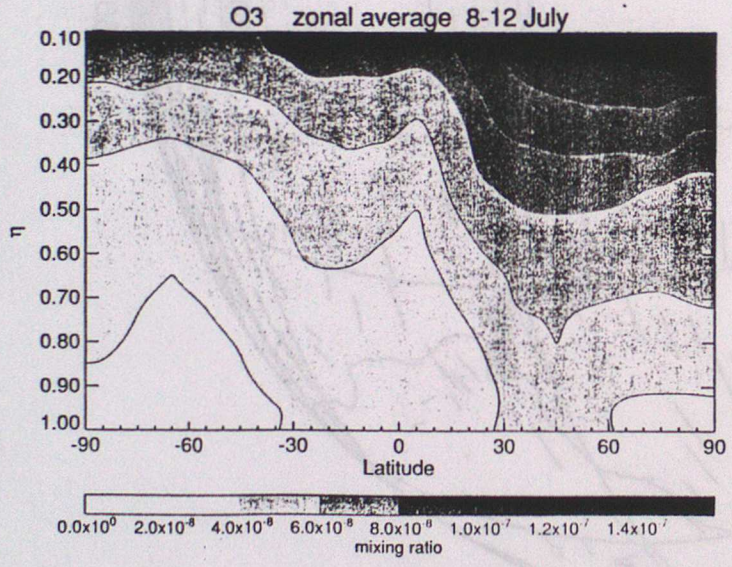

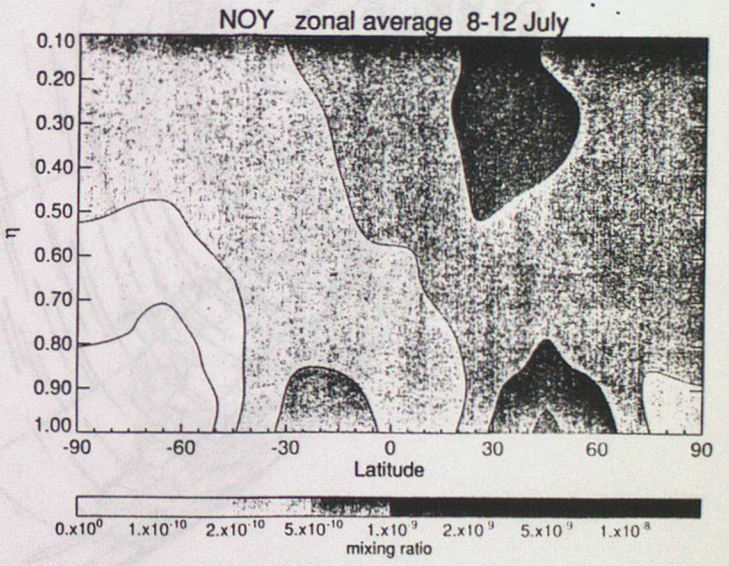

Fig. 2. Near surface and zonal average profiles of mixing ratios of OH, NO_y, HO_2 and O_3 after a 71 day run ending on 12th July. The values are the average mixing ratios over the last 5 days of the run.

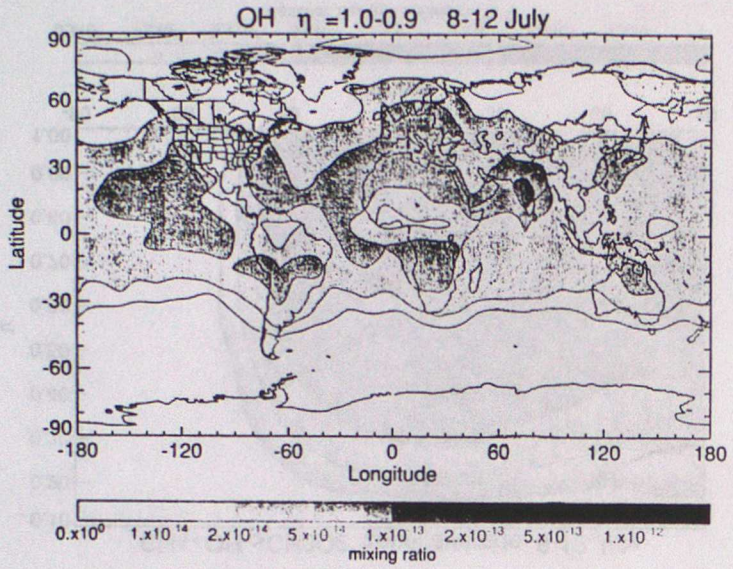

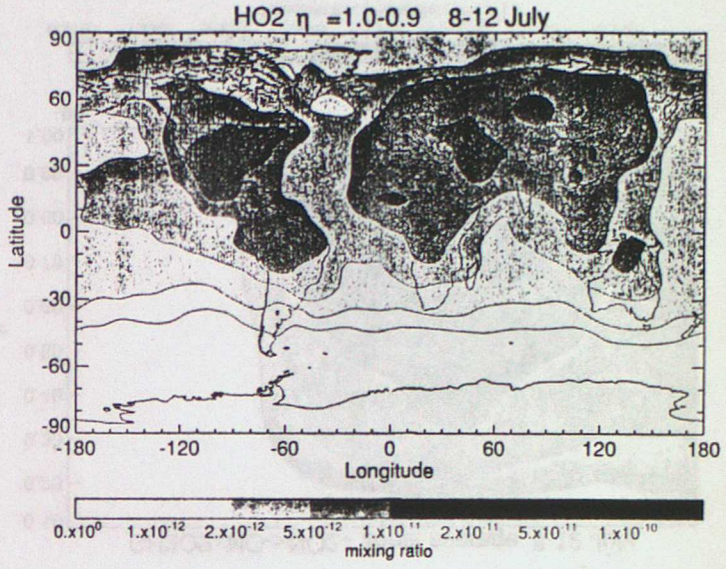

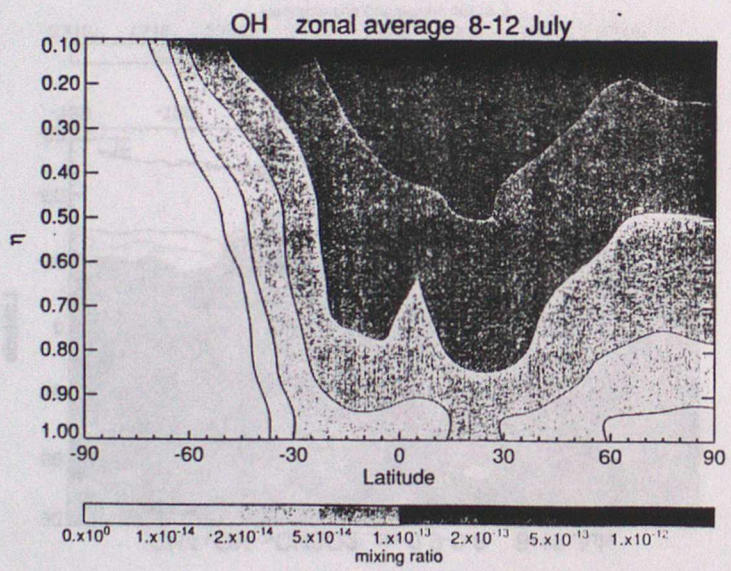

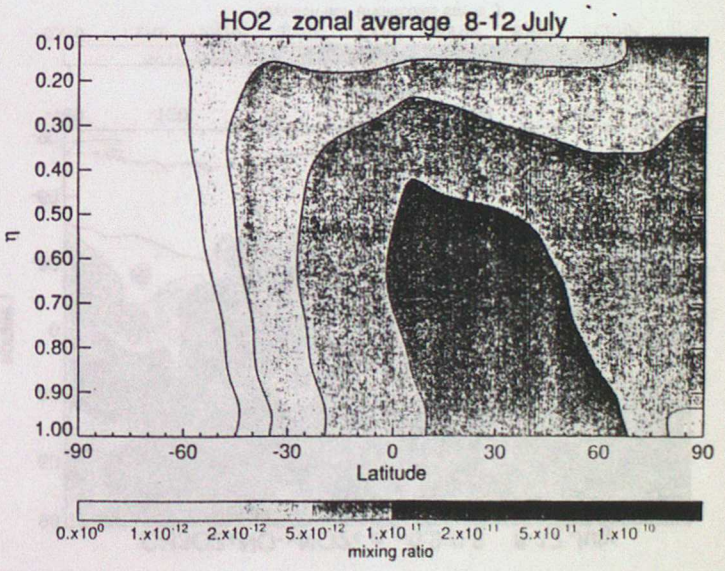

Fig. 3. Near surface and zonal average profiles of fluxes through the reactions $OH + CH_4 + O_2 \rightarrow CH_3O_2 + H_2O$ and $CH_3O_2 + NO + O_2 \rightarrow NO_2 + HO_2 + HCHO$ after a 71 day run ending on 12th July. The values are the average fluxes over the last 5 days of the run.

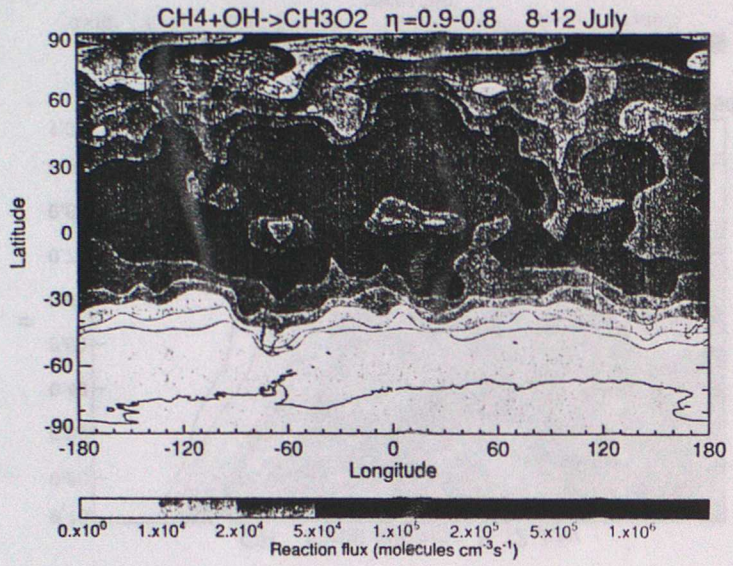

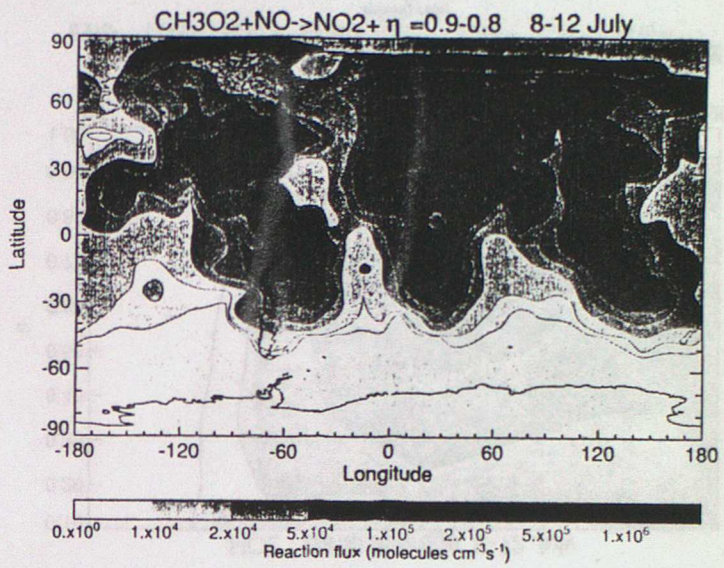

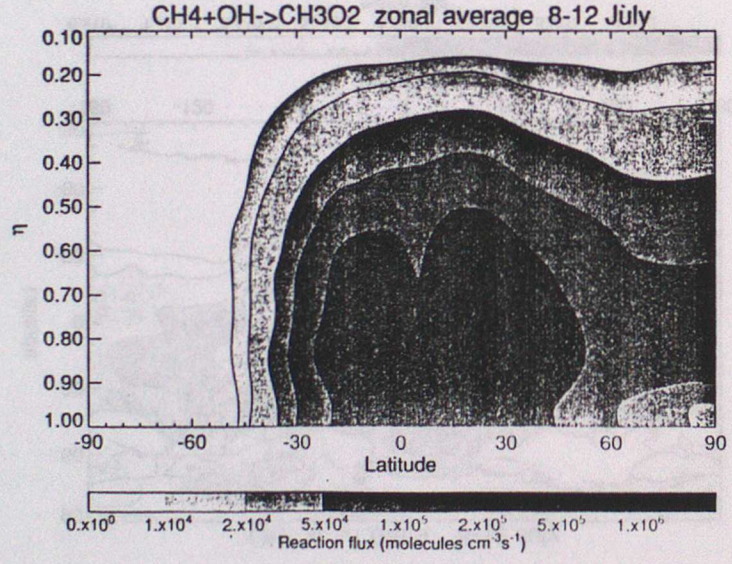

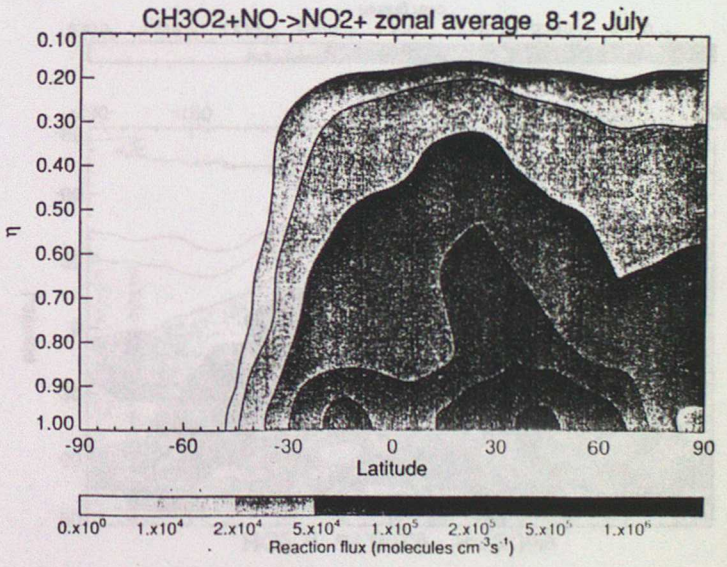

Fig. 4. Zonal average profiles of the OH molecular density: (a) after a 71 day run ending on 12th July, and (b) after a 70 day run ending on 5th February. The values are the averaged over the last 5 days of the run.

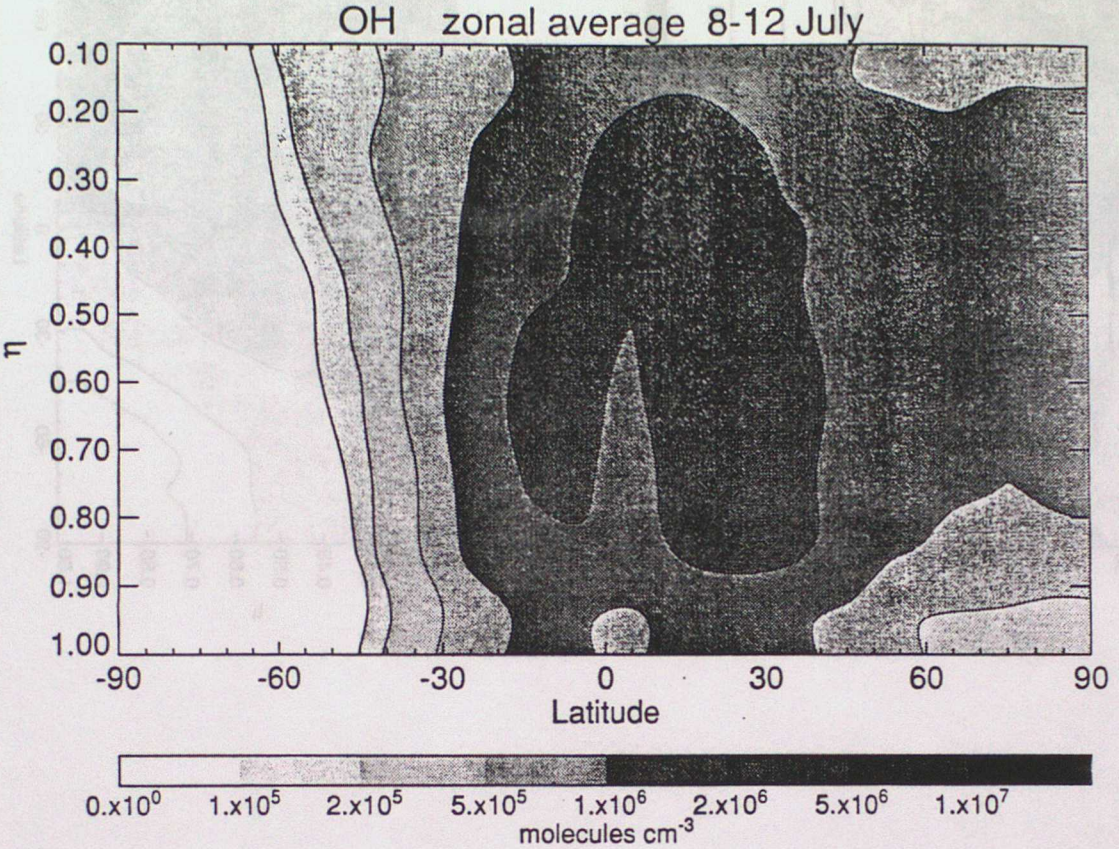

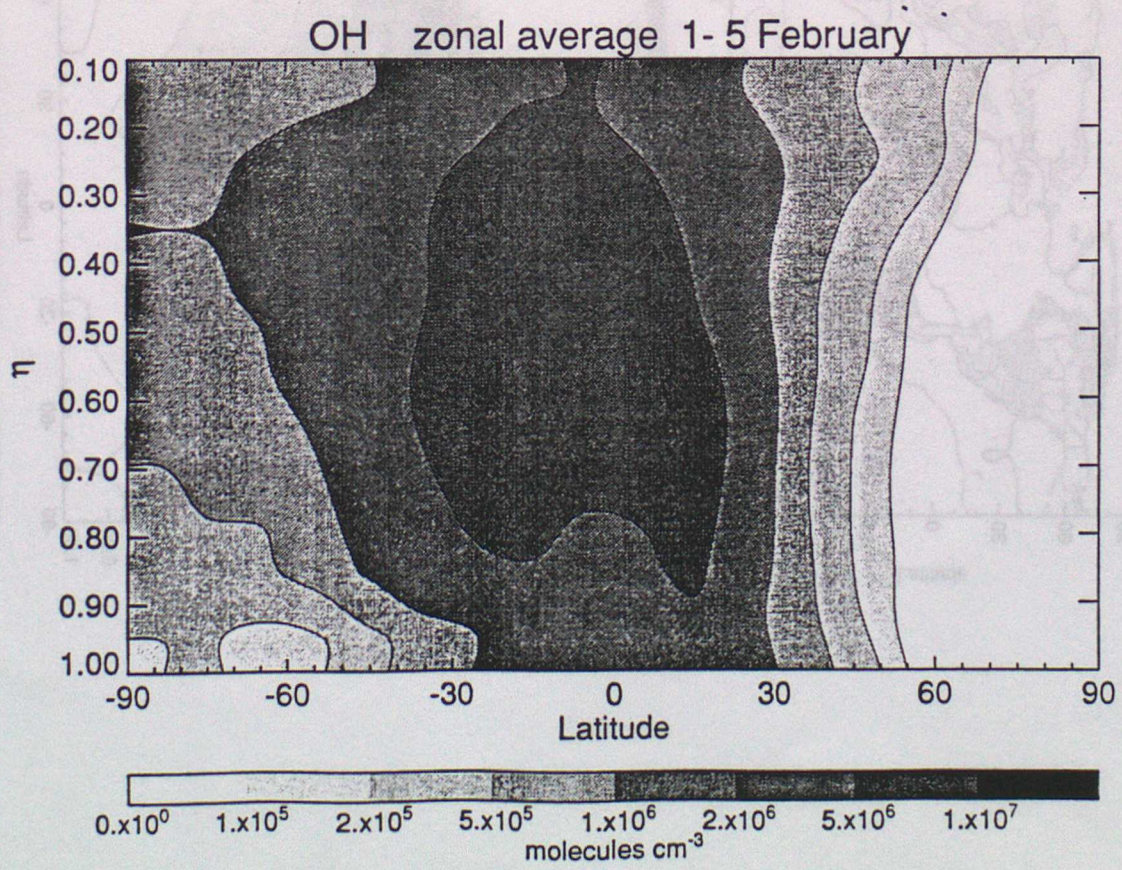

Fig. 5. Near surface mixing ratios of O_3, NO_Y, OH and HO_2 after a 70 day run ending on 2nd February using full European NO emissions. The values are the average mixing ratios over the previous 24 hours.

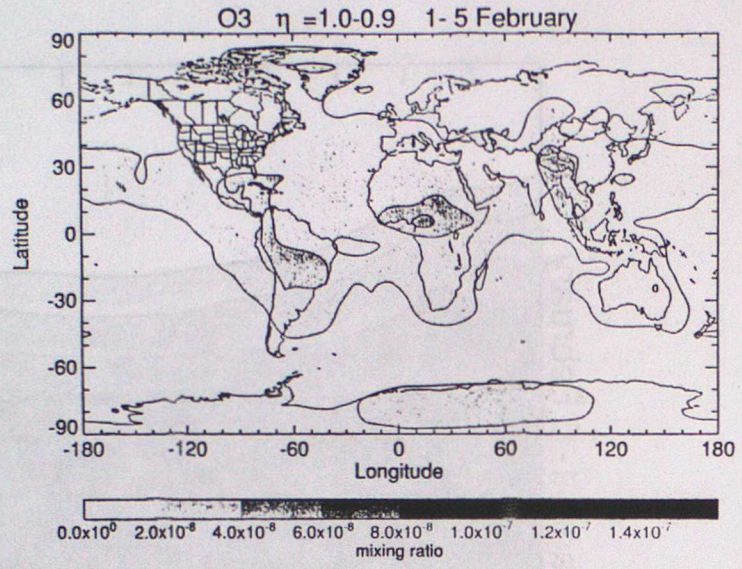

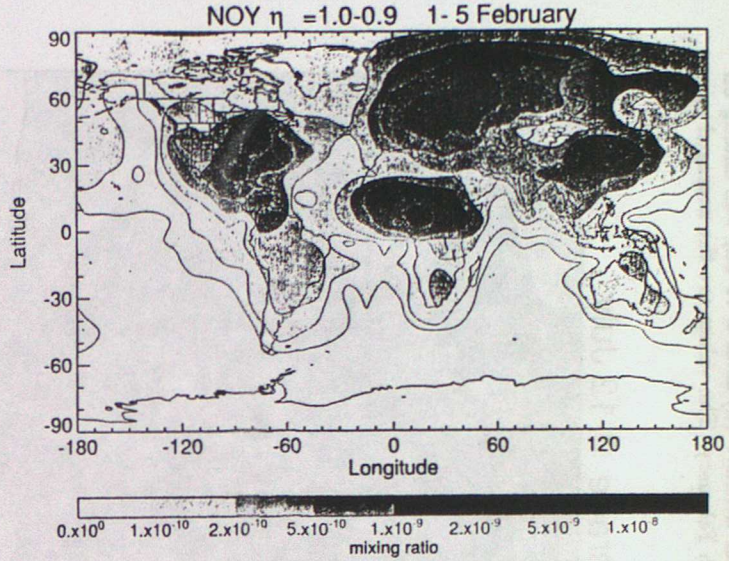

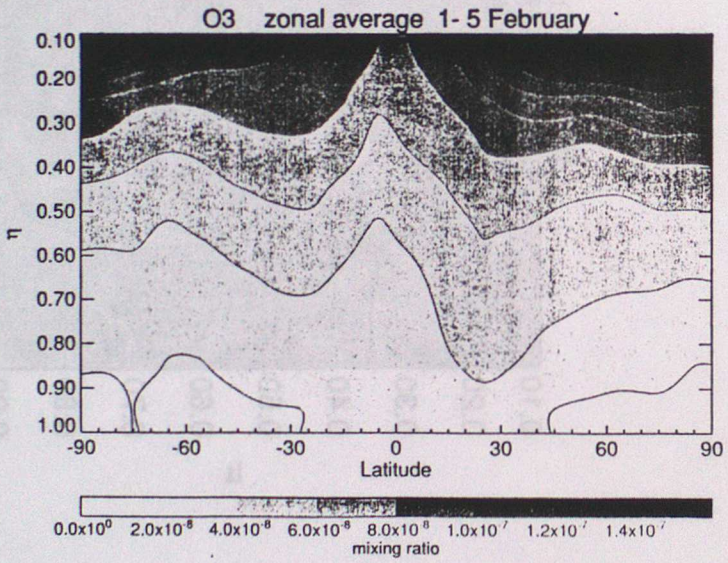

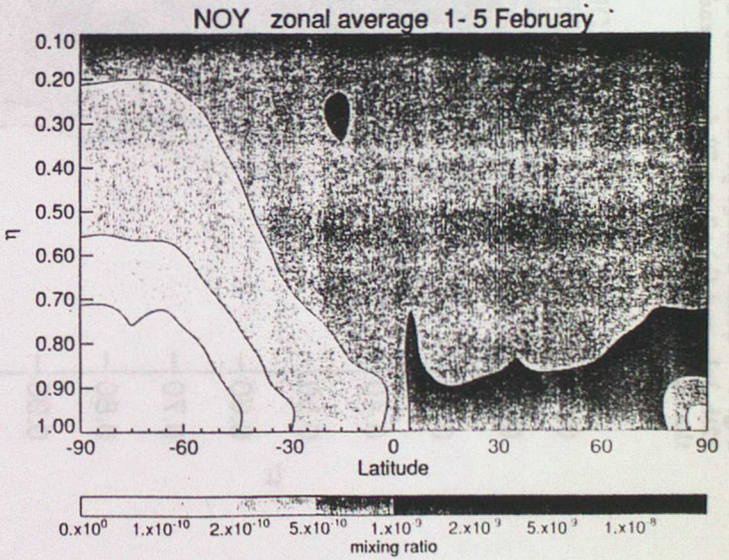

Fig. 5. Near surface mixing ratios of O_3, NO_3^-, OH and HO_2 after a 70 day run ending on 2nd February using full European NO emissions. The values are the average mixing ratios over the previous 24 hours.

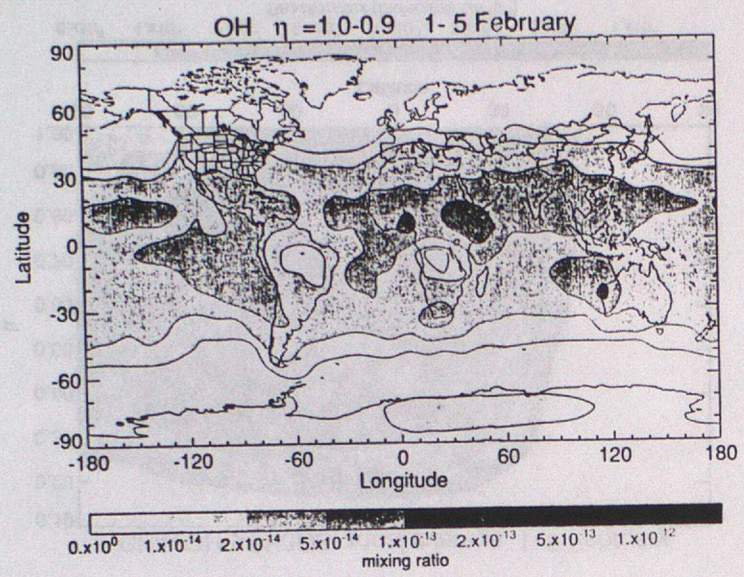

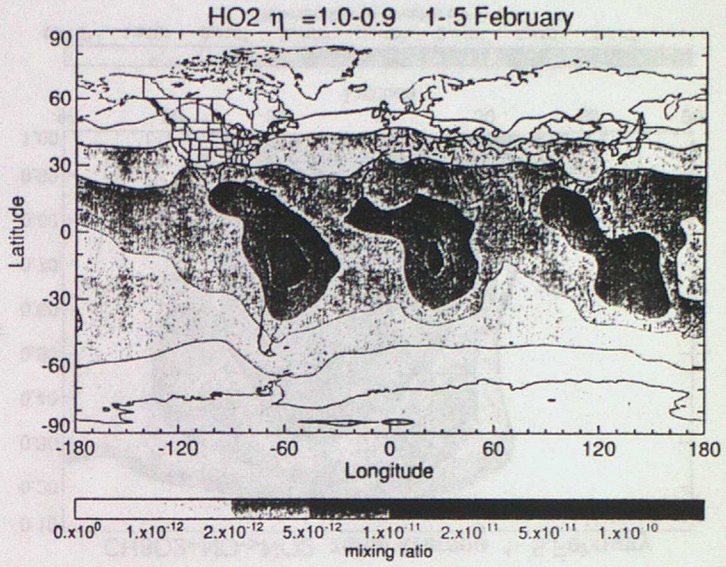

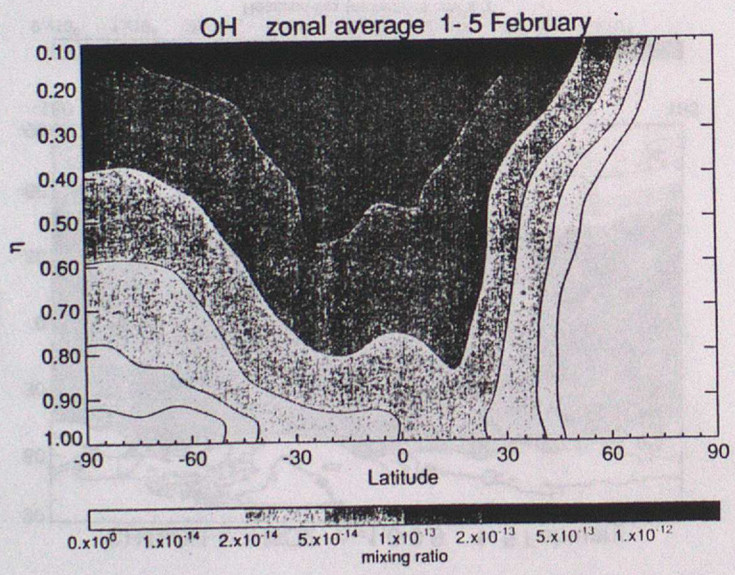

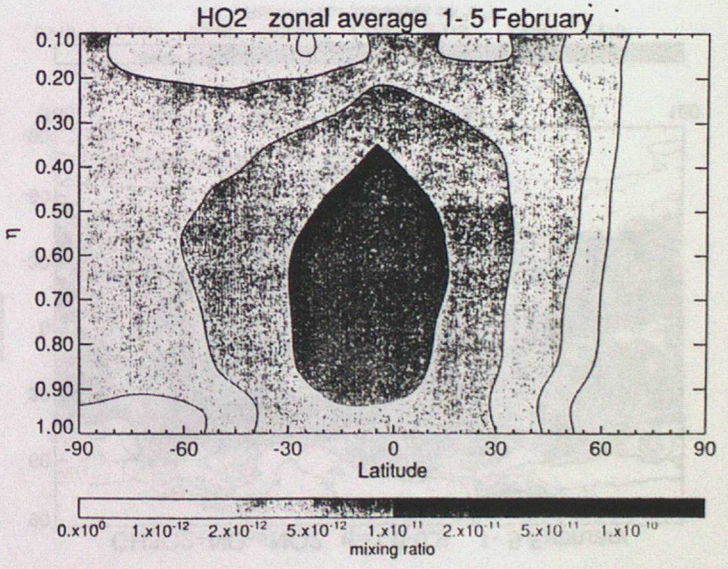

Fig. 6. Near surface and zonal average profiles of fluxes through the reactions $OH + CH_4 + O_2 \rightarrow CH_3O_2 + H_2O$ and $CH_3O_2 + NO + O_2 \rightarrow NO_2 + HO_2 + HCHO$ after a 70 day run ending on 5th February. The values are the average fluxes over the last 5 days of the run.

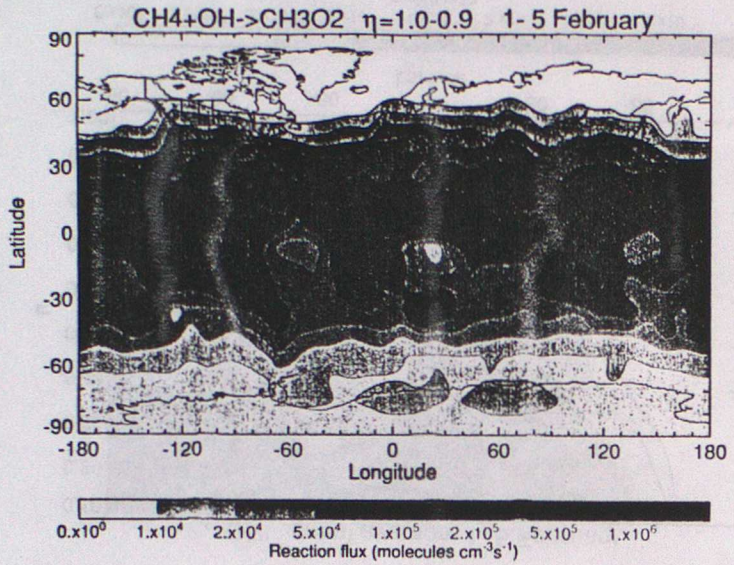

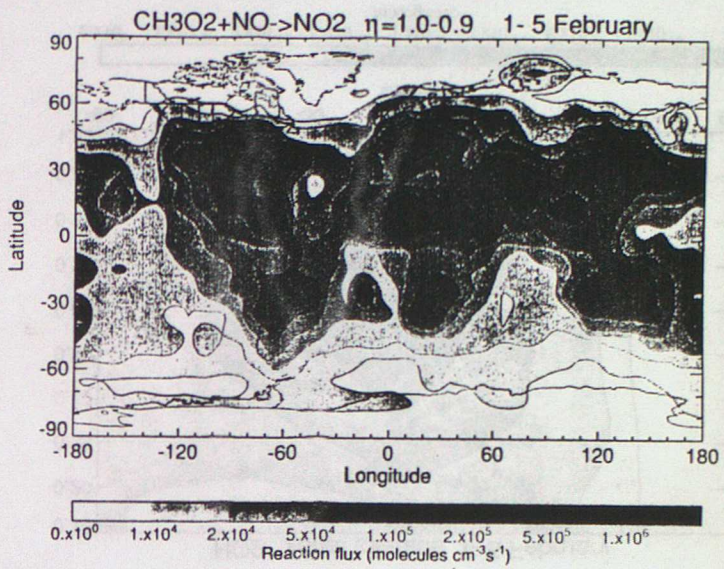

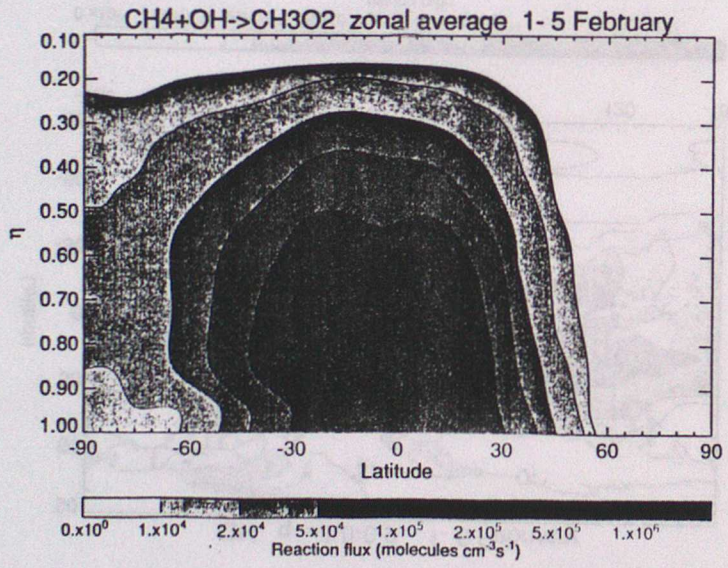

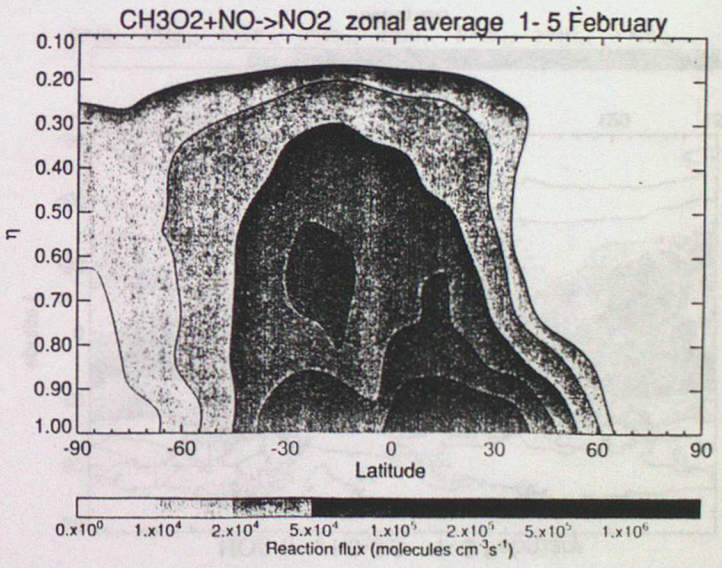

Fig. 7. Lifetimes of the hydrocarbons and other tropospheric trace gases in the 3-D model plotted against their OH + trace gas rate coefficients evaluated at 280 K.

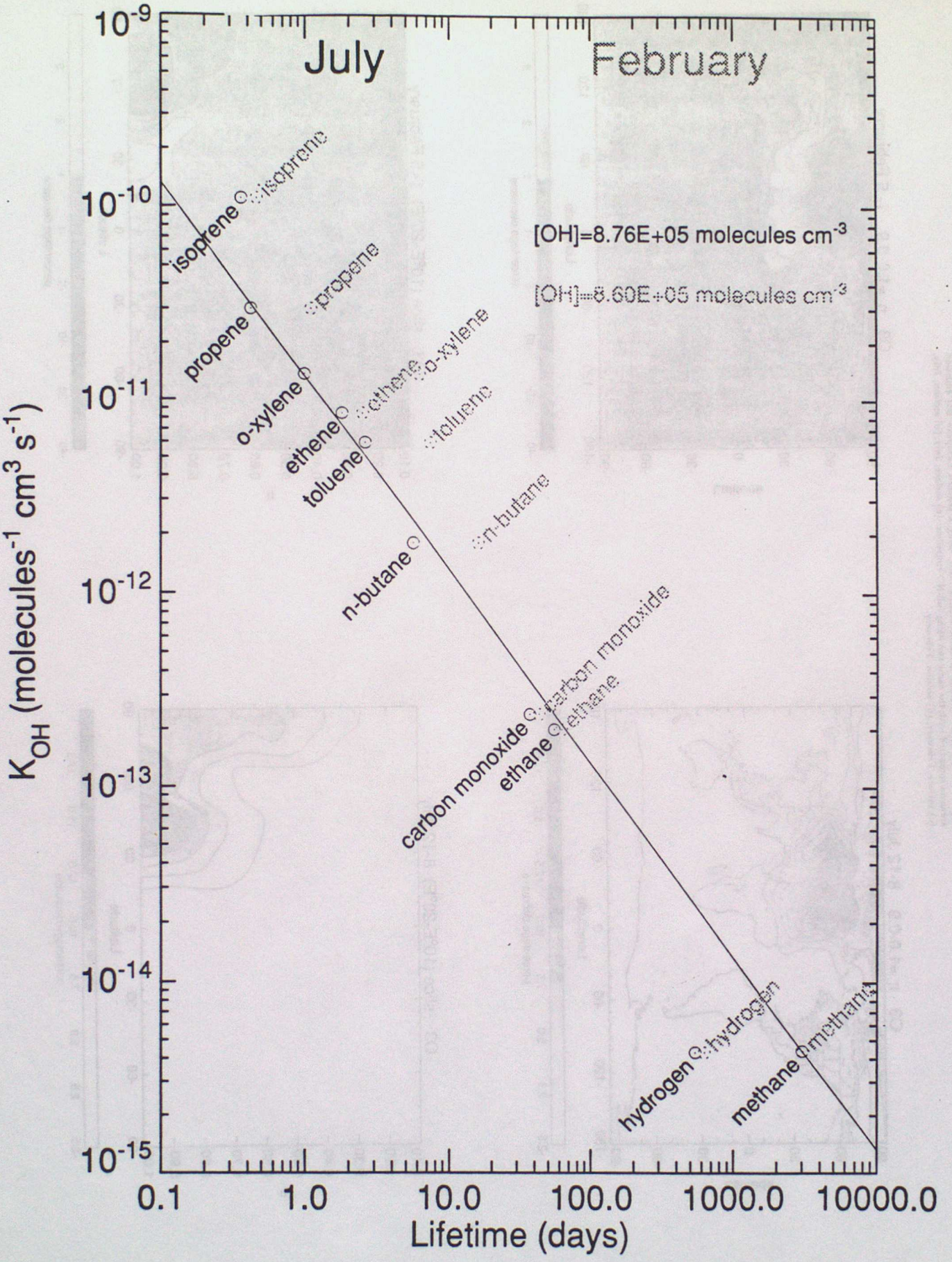

Fig. 8. Fractional decrease in ozone mixing ratio, using a reduced European NO emission scenario compared with the same run using full NO emissions: (a) surface, July, (b) section, July, (c) surface, February, (d) section, February.

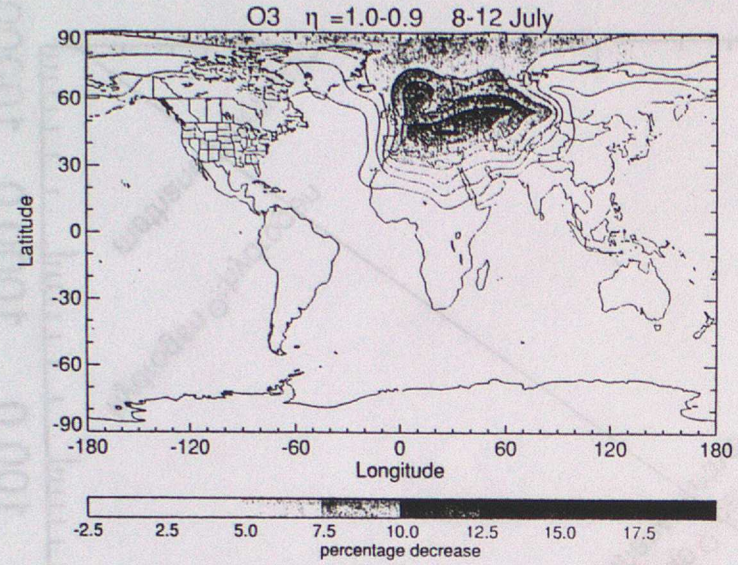

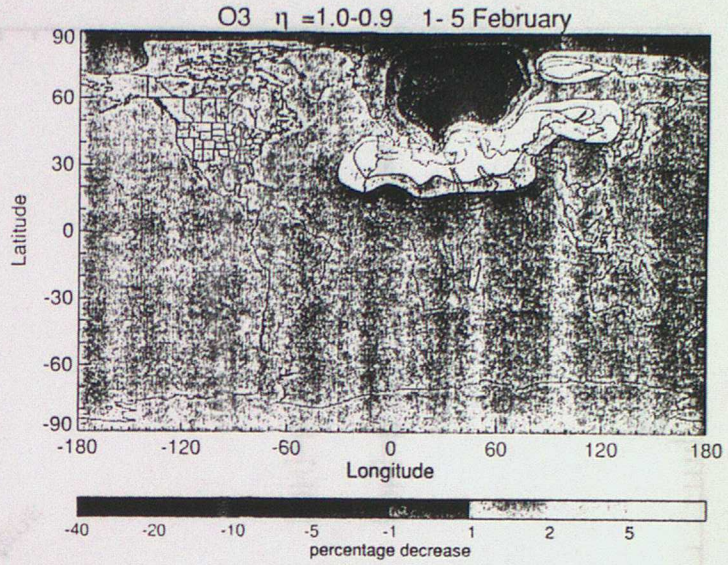

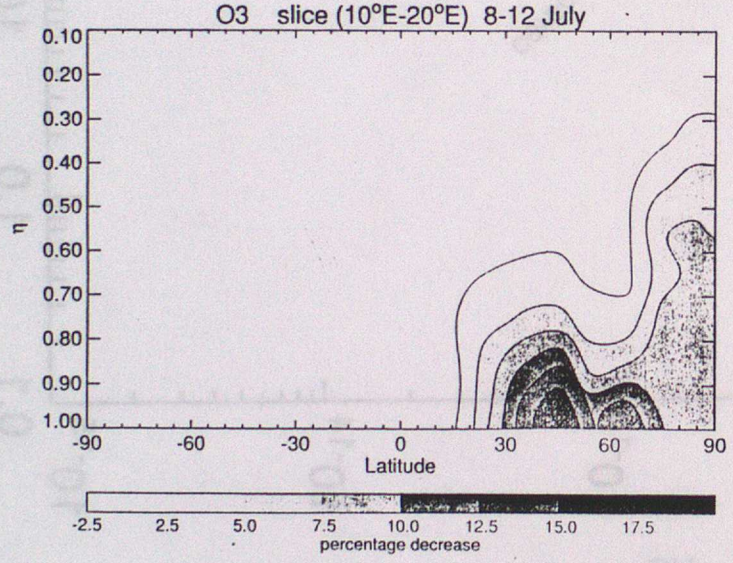

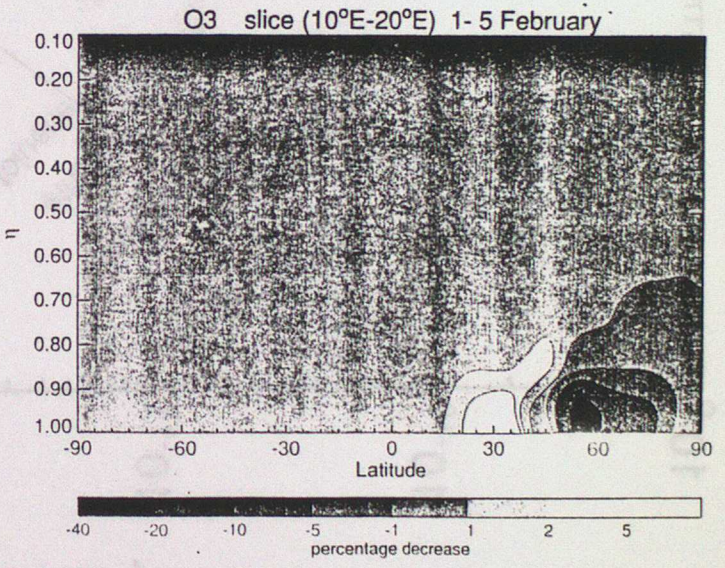

Fig. 9. Change in ozone mixing ratio divided by the change in NO_y mixing ratio, between the two runs with different NO emission scenarios: (a) surface, July, (b) section, July, (c) surface, February, (d) section, February. Only values where the NO_y mixing ratio has changed by more than 100 parts per trillion (100 ppt) are used.

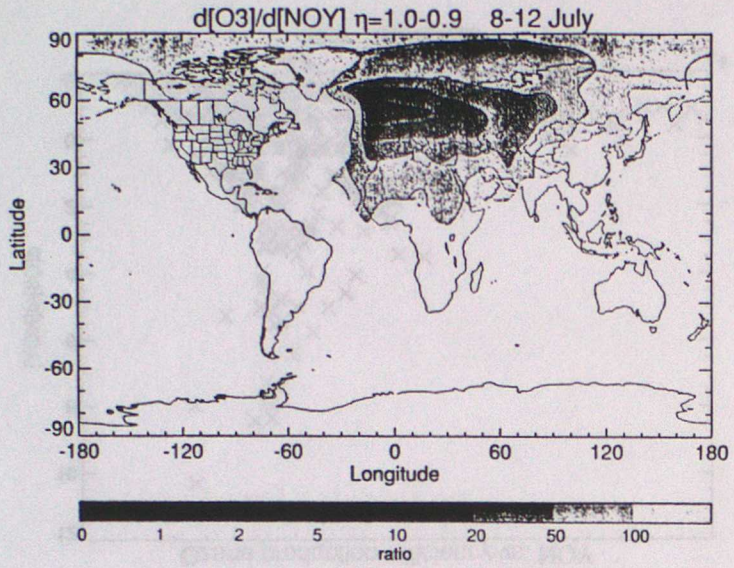

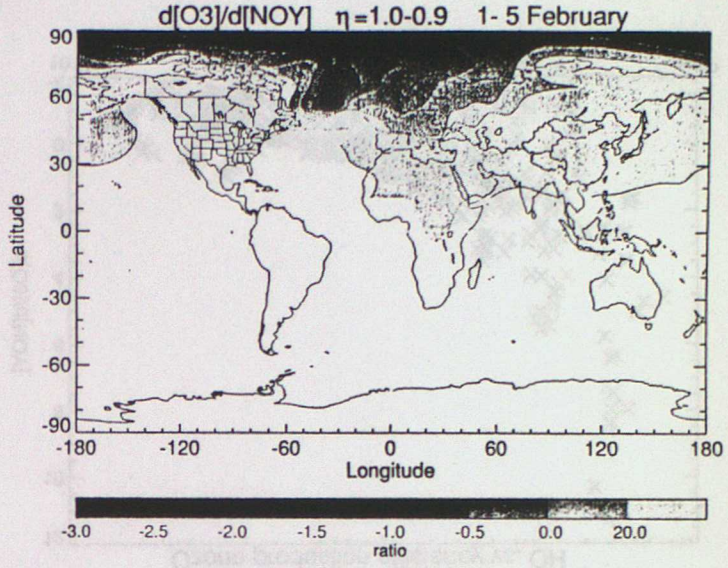

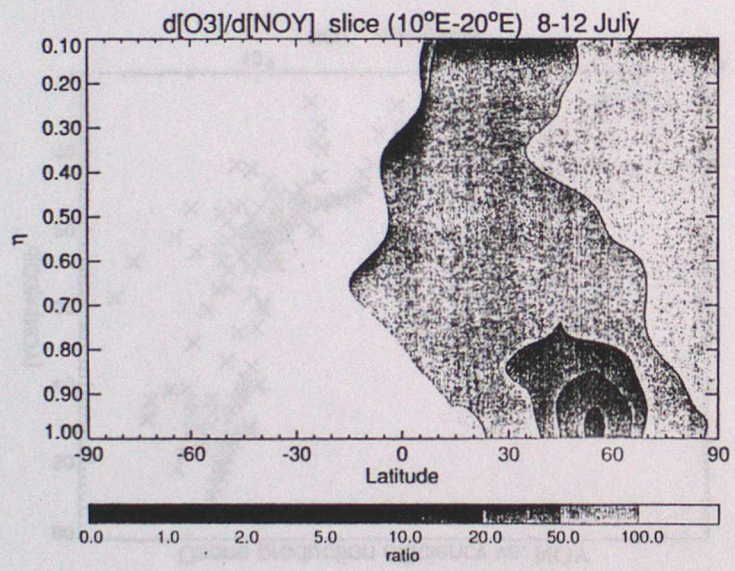

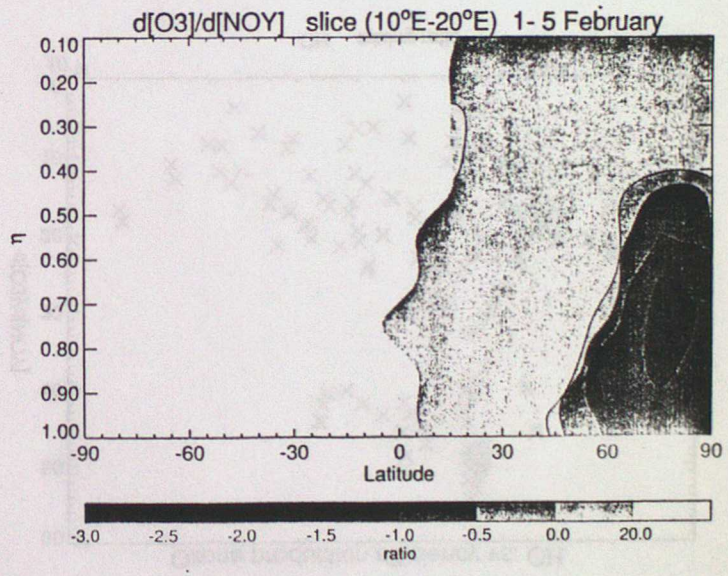

Fig. 10. Ozone production efficiency, defined as the change in ozone divided by the change in NO between the two runs, against the NO_y and OH mixing ratios without emission controls: (a) and (b) July, (c) and (d) February. Values plotted are for all the grid points where the change in NO_y mixing ratio was greater than 100 ppt.